Mixed and Nitsche's discretizations of Coulomb frictional contact-mechanics for mixed dimensional poromechanical models

Laurence Beaude, Franz Chouly, Mohamed Laaziri, Roland Masson

Mixed and Nitsche's discretizations of Coulomb frictional contact-mechanics for mixed dimensional poromechanical models

L. Beaude[*], F. Chouly[†], M. Laaziri[‡], R. Masson[§]

January 20, 2023

Abstract

This work deals with the discretization of single-phase Darcy flows in fractured and deformable porous media, including frictional contact at the matrix-fracture interfaces. Fractures are described as a network of planar surfaces leading to so-called mixed-dimensional models. Small displacements and a linear poro-elastic behavior are considered in the matrix. One key difficulty to simulate such coupled poro-mechanical models is related to the formulation and discretization of the contact mechanical sub-problem. Our starting point is based on the mixed formulation using facewise constant Lagrange multipliers along the fractures representing normal and tangential stresses. This is a natural choice for the discretization of the contact dual cone in order to account for complex fracture networks with corners and intersections. It leads to local expressions of the contact conditions and to efficient semi-smooth nonlinear solvers. On the other hand, such a mixed formulation requires to satisfy a compatibility condition between the discrete spaces restricting the choice of the displacement space and potentially leading to sub-optimal accuracy. This motivates the investigation of two alternative formulations based either on a stabilized mixed formulation or on the Nitsche's method. These three types of formulations are first investigated theoritically in order to enhance their connections. Then, they are compared numerically in terms of accuracy and nonlinear convergence. The sensitivity to the choice of the formulation parameters is also investigated. Several 2D test cases are considered with various fracture networks using both $\mathbb{P}_1$ and $\mathbb{P}_2$ conforming Finite Element discretizations of the displacement field and an Hybrid Finite Volume discretization of the mixed-dimensional Darcy flow model.

Keywords: Contact mechanics, Coulomb friction, Stabilized mixed method, Nitsche's method, Poromechanics, Discrete Fracture Matrix model.

[*]BRGM, Orléans, laurence.beaude@brgm.fr

[†]Université de Bourgogne, Institut de Mathématiques de Bourgogne, 21078 Dijon, France – Center for Mathematical Modeling and Department of Mathematical Engineering, University of Chile and IRL 2807 – CNRS, Santiago, Chile – Departamento de Ingeniería Matemática, CI^{2}MA, Universidad de Concepción, Casilla 160-C, Concepción, Chile, franz.chouly@u-bourgogne.fr

[‡]Université Côte d'Azur, Inria, CNRS, LJAD, UMR 7351 CNRS, team Coffee, Parc Valrose 06108 Nice Cedex 02, France, mohamed.laaziri@univ-cotedazur.fr

[§]Université Côte d'Azur, Inria, CNRS, LJAD, UMR 7351 CNRS, team Coffee, Parc Valrose 06108 Nice Cedex 02, France, roland.masson@univ-cotedazur.fr

1 Introduction

Coupled flow and geomechanics in fractured porous media play an important role in many subsurface applications. This is typically the case of CO_2 storage, for which fault reactivation that can result from CO_2 injection must be avoided to preserve the storage integrity. On the other hand, in enhanced geothermal systems, fracture conductivity must be increased by hydraulic stimulation to produce heat while avoiding the risk of induced seismicity. Such processes couple the flow in the porous medium and the fractures, the poromechanical deformation of the porous rock and the mechanical behavior of the fractures.

Their mathematical modeling is typically based on mixed-dimensional geometries representing the fractures as a network of codimension one surfaces. The model combines first the mixed-dimensional flow model, coupling typically a Poiseuille flow along the network of fractures with the Darcy flow in the surrounding porous rock called the matrix [2, 26, 42, 45, 3, 53, 50, 16, 17, 14, 27, 19, 47, 7]. The second ingredient of the model is based on poromechanics, coupling the rock deformation with the Darcy flow in the matrix domain. Let us refer to the monograph [25] as a reference textbook on this topic. In the following we will assume small strains and porosity variations as well as a poro-elastic mechanical behavior of the porous rock. The third ingredient of the fully coupled model is related to the mechanical behavior of the fractures given the matrix mechanical deformation and the matrix and fracture fluid pressures. It is typically based on contact mechanics governing the contact and slip conditions [43, 56, 54]. Note also that fractures are assumed to pre-exist and that fracture propagation is not addressed here.

The modeling and numerical simulation of such mixed-dimensional poromechanical models have been the object of many recent works [28, 29, 30, 6, 51, 9, 10, 12, 13]. In terms of discretizations, they are mostly based on conservative finite volume schemes for the flow and use either a conforming finite element method [28, 29, 30, 12] or a finite volume scheme for the mechanics [6, 51]. Note that the saddle point nature of the coupling between the matrix fluid pressure and the displacement field requires a compatibility condition between both discretizations, as in [6, 51, 9, 10, 12], or alternatively additional stabilization terms to get the stability of the pressure solution in the limit of low rock permeability, incompressible fluid and small times.

The contact mechanics formulation is a key ingredient to efficiently handle the non-linear variational inequalities of the contact fracture model. It is typically either based on a mixed formulation with Lagrange multipliers to impose the contact conditions as in [28, 6, 51, 12] or on a consistent Nitsche's penalization method as in [30] (see also [18] for a recent alternative approach based on PDE control). Again, if a mixed formulation is used, a compatibility condition must be satisfied between the Lagrange multiplier and displacement field spaces [6, 51, 12] or a stabilization must be specifically designed [28].

Nitsche's method has been considered only recently to discretize contact and friction conditions, despite the fact that it has gained popularity for other boundary conditions. The Nitsche's method orginally proposed in [46] aims at treating the boundary or interface conditions in a weak sense, with appropriate consistent terms that involve only the primal variables. It differs in this aspect from standard penalization techniques which are generally non-consistent [43]. Moreover, no additional unknown (Lagrange multiplier) is needed and,

therefore, no discrete inf–sup condition must be fulfilled, contrarily to mixed methods (see, *e.g.*, [37, 54]). In some previous works [36, 39] it has been adapted for bilateral (persistent) contact, which still corresponds to linear boundary conditions on the contact zone. We remark furthermore that an algorithm for unilateral contact which makes use of Nitsche's method in its original form is presented and implemented in [36], In [22, 24] a new Nitsche-based Finite Element method was proposed and analyzed for Signorini's problem, where a linear elastic body is in frictionless contact with a rigid foundation. Conversely to bilateral (persistent) contact, Signorini's problem involves non-linear boundary conditions associated to unilateral contact, with an unknown actual contact region. The extension to the Tresca friction model is analysed in [20] and to the Coulomb friction model in [23]. Following the pioneering paper of R. Stenberg [52], various recent works have been dedicated to improve our understanding of the link between Nitsche's and stabilized mixed methods: see [33] for domain decomposition, see [32, 34] for frictionless contact and [35] for Tresca friction. Very few works exist related to Nitsche's method for contact and friction in the context of fracture mechanics. Let us mention however [29], where the iterative method of [36] is adapted for the approximate solution of contact in fractures.

Moreover the Nitsche-based Finite Element method encompasses symmetric and nonsymmetric variants depending upon a parameter called θ. The symmetric case of [22] is recovered when $\theta = 1$. When $\theta \neq 1$ positivity of the contact term in the Nitsche's variational formulation is generally lost. Nevertheless some other advantages are recovered, mostly from the numerical viewpoint. Namely, one of the variants ($\theta = 0$) involves a reduced quantity of terms, which makes it easier to implement and to extend to contact problems involving non-linear elasticity. In addition, this nonsymmetric variant $\theta = 0$ performs better in the sense it requires less Newton iterations to converge, for a wider range of the Nitsche's parameter, than the variant $\theta = 1$, see [49]. Concerning the skew-symmetric variant $\theta = -1$, the well-posedness of the discrete formulation and the optimal convergence are preserved irrespectively of the value of the Nitsche's parameter.

This work investigates both mixed and Nitsche's formulations of the contact mechanics for mixed-dimensional poro-elastic problems. We focus on the mixed formulation based on a facewise constant approximation of the Lagrange multipliers. This allows to deal readily with fracture intersections, corners and tips still leading to local expressions of the discrete contact conditions and efficient non-linear solvers based on semi-smooth Newton algorithms [54]. On the other hand, the mixed formulation requires an inf-sup compatibility conditions between the displacement and the Lagrange multiplier discrete spaces which is typically not satisfied for the first order Finite Element discretization. Following [44, 41], this restriction can be circumvented using a stabilized mixed formulation based on an extension to contact boundary conditions of the pioneer work [4]. Furthermore, exploiting their facewise constant approximation, the Lagrange multipliers can be eliminated. It leads to a new Nistche type method (called hereafter the mean-Nitsche's method) based on face average tractions and displacement jumps, bridging the gap between the Nitsche method introduced in [24, 20, 23] and the mixed formulation (see also the related works [32, 34, 35]). The links between the mixed and mean-Nitsche's formulations of the contact mechanics are carefully investigated in this work. Then, a numerical comparison of the three approaches is performed, both in terms of accuracy and in terms of robustness of the non-linear solvers based on semi-smooth Newton algorithms. The stand alone mechanical problem with Coulomb frictional contact at matrix fracture interfaces is first considered on 2D test cases with various fracture networks.

Both the $\mathbb{P}_1$ and $\mathbb{P}_2$ Finite Element approximations of the displacement field are tested. We also investigate the sensitivity of the algorithms to their parameters, namely the Nitsche's and mean-Nitsche's stabilization and θ parameters, as well as the parameters of the semi-smooth Newton algorithm for the mixed formulation. Finally, the three formulations of the contact mechanics are compared on a coupled poro-elastic 2D test case with a network of fractures based on the test case presented in [6].

The remainder of the paper is organized as follows. In Section 2, the mixed-dimensional poro-elastic model is described starting with the geometry and function spaces in Subsection 2.1 followed by the physical model coupling the flow, the poro-elastic and the Coulomb frictional contact models in Subsection 2.2. The three discretizations of the contact mechanical model are presented in Section 3. The mixed formulation is first recalled in Section 3.1, then we introduce the stabilized mixed discretization and carefully investigate its mean-Nitsche's equivalent formulation in Subsection 3.2 as well as its links with the mixed formulation. The Nitsche's discretization introduced in [24, 20, 23] is recalled in Subsection 3.3. Section 4 compares the performance of the three discretizations on stand alone contact mechanical test cases with various fracture networks. In Section 5, the comparison is extended to a coupled mixed-dimensional poro-elastic test case. Section 6 draws the conclusions and perspectives of this work.

2 Mixed-dimensional poromechanical model with contact mechanics

First we present the geometrical setting and then we provide the poromechanical model in strong form.

2.1 Mixed-dimensional geometry and function spaces

In what follows, scalar fields are represented by lightface letters, vector fields by boldface letters. We use the overline notation $\overline{v}$ to distinguish an exact (scalar or vector) field from its discrete counterpart v. We let $\Omega \subset \mathbb{R}^d$, $d \in \{2, 3\}$, denote a bounded polytopal domain, partitioned into a fracture domain Γ and a matrix domain $\Omega \backslash \overline{\Gamma}$. The network of fractures is defined by

$$\overline{\Gamma} = \bigcup_{i \in I} \overline{\Gamma}_i,$$

where each fracture $\Gamma_i \subset \Omega$, $i \in I$ is a planar polygonal simply connected open domain. Without restriction of generality, we will assume that the fractures may only intersect at their boundaries (Figure 1), that is, for any $i, j \in I, i \neq j$ it holds $\Gamma_i \cap \Gamma_j = \varnothing$, but not necessarily $\overline{\Gamma}_i \cap \overline{\Gamma}_j = \varnothing$.

The two sides of a given fracture of Γ are denoted by $\pm$ in the matrix domain, with unit normal vectors $\mathbf{n}^{\pm}$ oriented outward from the sides $\pm$. We denote by $\gamma_{\mathfrak{a}}$ the trace operators on the side $\mathfrak{a} \in \{+, -\}$ of Γ for functions in $H^1(\Omega \backslash \overline{\Gamma})$ and by $\gamma_{\partial\Omega}$ the trace operator for the same functions on $\partial\Omega$. The jump operator on Γ for functions $\overline{\mathbf{u}}$ in $(H^1(\Omega \backslash \overline{\Gamma}))^d$ is defined by

$$[\![\overline{\mathbf{u}}]\!] = \gamma_+ \overline{\mathbf{u}} - \gamma_- \overline{\mathbf{u}},$$

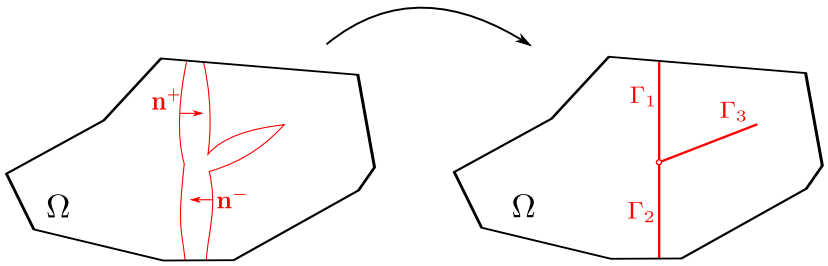

Figure 1: Illustration of the dimension reduction in the fracture aperture for a 2D domain Ω with three intersecting fractures Γ_i, $i \in \{1,2,3\}$, with the equi-dimensional geometry on the left and the mixed-dimensional geometry on the right.

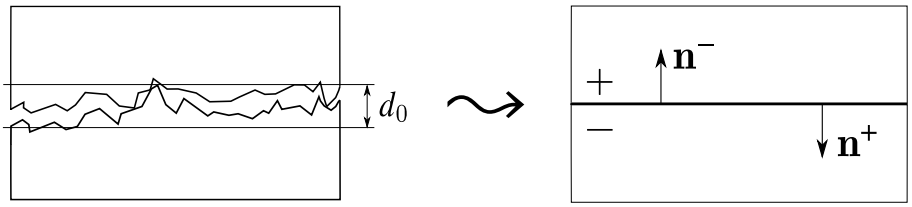

Figure 2: Conceptual fracture model with contact at asperities, d_0 being the fracture aperture at contact state.

and we denote by

$$[\![\overline{\mathbf{u}}]\!]_n = [\![\overline{\mathbf{u}}]\!] \cdot \mathbf{n}^+ \quad \text{and} \quad [\![\overline{\mathbf{u}}]\!]_\tau = [\![\overline{\mathbf{u}}]\!] - [\![\overline{\mathbf{u}}]\!]_n \mathbf{n}^+$$

its normal and tangential components. The tangential gradient and divergence along the fractures are respectively denoted by ∇_τ and div_τ. The symmetric gradient operator $\mathfrak{e}$ is defined such that $\mathfrak{e}(\overline{\mathbf{v}}) = \frac{1}{2}(\nabla\overline{\mathbf{v}} + (\nabla\overline{\mathbf{v}})^t)$ for a given vector field $\overline{\mathbf{v}} \in H^1(\Omega\backslash\overline{\Gamma})^d$.

Let us denote by $d_0 : \Gamma \to (0, +\infty)$ the fracture aperture in the contact state (see Figure 2). The function d_0 is assumed to be continuous with zero limits at $\partial\Gamma\backslash(\partial\Gamma \cap \partial\Omega)$ (i.e. the tips of Γ) and strictly positive limits at $\partial\Gamma \cap \partial\Omega$.

Let us introduce some relevant function spaces. $H^1_{d_0}(\Gamma)$ is the space of functions $v_\Gamma \in L^2(\Gamma)$ such that $d_0^{3/2}\nabla_\tau v_\Gamma$ belongs to $L^2(\Gamma)^{d-1}$, and whose traces are continuous at fracture intersections $\partial\Gamma_i \cap \partial\Gamma_j$ (for $(i,j) \in I \times I$, $i \neq j$) and vanish on the boundary $\partial\Gamma \cap \partial\Omega$. The weight $d_0^{3/2}$ in the definition of $H^1_{d_0}(\Gamma)$ accounts for the fact that $\overline{d}_f \geqslant d_0$ can vanish at the tips and that only the $L^2(\Gamma)^{d-1}$ norm of $\overline{d}_f^{3/2}\nabla_\tau\overline{p}_f$ will be controlled, where $\overline{p}_f$ is the fracture pressure along the fractures. The space for the displacement is

$$\mathbf{U}_0 = \{\overline{\mathbf{v}} \in (H^1(\Omega\backslash\overline{\Gamma}))^d : \gamma_{\partial\Omega}\overline{\mathbf{v}} = 0\},$$

endowed with the norm $\|\overline{\mathbf{v}}\|_{\mathbf{U}_0} = \|\nabla\overline{\mathbf{v}}\|_{L^2(\Omega)^d}$. The space for the pair of matrix/fracture pressures is

$$V^0 = V_m^0 \times V_f^0 \quad \text{with} \quad V_m^0 = \{\overline{v} \in H^1(\Omega\backslash\overline{\Gamma}) \ : \ \gamma_{\partial\Omega}\overline{v} = 0\} \ \text{ and } \ V_f^0 = H^1_{d_0}(\Gamma).$$

For $\overline{v} = (\overline{v}_m, \overline{v}_f) \in V^0$, let us denote the jump operator on the side $\mathfrak{a} \in \{+,-\}$ of the fracture by

$$[\![\overline{v}]\!]_\mathfrak{a} = \gamma_\mathfrak{a}\overline{v}_m - \overline{v}_f.$$

Finally, for any $x \in \mathbb{R}$, we set $x^+ = \max\{0, x\}$ and $x^- = (-x)^+$.

2.2 Problem statement

The primary unknowns of the coupled model in its strong form are the matrix and fracture pressures $\overline{p}_\omega$, $\omega \in \{m, f\}$ and the displacement vector field $\overline{\mathbf{u}}$. The coupled problem is formulated in terms of flow model, contact mechanics model together with coupling conditions. The flow model is a mixed-dimensional model assuming an incompressible fluid. It accounts for the volume conservation equations and for the Darcy and Poiseuille laws defining respectively the velocity fields $\overline{\mathbf{q}}_m$ in the matrix and $\overline{\mathbf{q}}_f$ along the fractures:

$$\begin{cases} \partial_t \overline{\phi}_m + \operatorname{div}(\overline{\mathbf{q}}_m) = 0 & \text{in } (0,T)\times\Omega\backslash\overline{\Gamma}, \\ \overline{\mathbf{q}}_m = -\dfrac{\mathbb{K}_m}{\eta}\nabla\overline{p}_m & \text{in } (0,T)\times\Omega\backslash\overline{\Gamma}, \\ \partial_t \overline{d}_f + \operatorname{div}_\tau(\overline{\mathbf{q}}_f) - \overline{\mathbf{q}}_m\cdot\mathbf{n}^+ - \overline{\mathbf{q}}_m\cdot\mathbf{n}^- = 0 & \text{in } (0,T)\times\Gamma, \\ \overline{\mathbf{q}}_f = -\dfrac{1}{12}\dfrac{\overline{d}_f^3}{\eta}\nabla_\tau\overline{p}_f & \text{in } (0,T)\times\Gamma. \end{cases} \tag{1a}$$

In (1a), the constant fluid dynamic viscosity is denoted by η, the matrix porosity by $\overline{\phi}_m$ and the matrix permeability tensor by $\mathbb{K}_m$. The fracture aperture, denoted by $\overline{d}_f$, yields the fracture conductivity $\frac{1}{12}\overline{d}_f^3$ *via* the Poiseuille law.

The quasi static contact mechanical model accounts for the poromechanical equilibrium equation with a Biot linear elastic constitutive law and a Coulomb frictional contact model at matrix–fracture interfaces:

$$\begin{cases} -\operatorname{div}\Big(\boldsymbol{\sigma}(\overline{\mathbf{u}}) - b\,\overline{p}_m\mathbb{I}\Big) = \mathbf{f} & \text{on } (0,T)\times\Omega\backslash\overline{\Gamma}, \\ \boldsymbol{\sigma}(\overline{\mathbf{u}}) = \frac{E}{1+\nu}\Big(\boldsymbol{\varepsilon}(\overline{\mathbf{u}}) + \frac{\nu}{1-2\nu}(\operatorname{div}\overline{\mathbf{u}})\mathbb{I}\Big) & \text{on } (0,T)\times\Omega\backslash\overline{\Gamma}, \\ \mathbf{T}^+(\overline{\mathbf{u}}) + \mathbf{T}^-(\overline{\mathbf{u}}) = \mathbf{0} & \text{on } (0,T)\times\Gamma, \\ T_n(\overline{\mathbf{u}}) \leqslant 0,\ [\![\overline{\mathbf{u}}]\!]_n \leqslant 0,\ [\![\overline{\mathbf{u}}]\!]_n\, T_n(\overline{\mathbf{u}}) = 0 & \text{on } (0,T)\times\Gamma, \\ |\mathbf{T}_\tau(\overline{\mathbf{u}})| \leqslant -F\, T_n(\overline{\mathbf{u}}) & \text{on } (0,T)\times\Gamma, \\ (\partial_t[\![\overline{\mathbf{u}}]\!]_\tau)\cdot\mathbf{T}_\tau(\overline{\mathbf{u}}) - F\, T_n(\overline{\mathbf{u}})|\partial_t[\![\overline{\mathbf{u}}]\!]_\tau| = 0 & \text{on } (0,T)\times\Gamma. \end{cases} \tag{1b}$$

In (1b), b is the Biot coefficient, E and ν are the effective Young modulus and Poisson ratio, $F \geqslant 0$ is the friction coefficient, and the contact tractions are defined by

$$\begin{cases} \mathbf{T}^{\mathfrak{a}}(\overline{\mathbf{u}}) = (\boldsymbol{\sigma}(\overline{\mathbf{u}}) - b\,\overline{p}_m\mathbb{I})\mathbf{n}^{\mathfrak{a}} + \overline{p}_f\mathbf{n}^{\mathfrak{a}}, \quad \mathfrak{a} \in \{+,-\}, \\ \mathbf{T}(\overline{\mathbf{u}}) = \mathbf{T}^+(\overline{\mathbf{u}}), \\ T_n(\overline{\mathbf{u}}) = \mathbf{T}^+(\overline{\mathbf{u}})\cdot\mathbf{n}^+, \\ \mathbf{T}_\tau(\overline{\mathbf{u}}) = \mathbf{T}^+(\overline{\mathbf{u}}) - (\mathbf{T}^+(\overline{\mathbf{u}})\cdot\mathbf{n}^+)\mathbf{n}^+. \end{cases}$$

The complete system of equations (1a)–(1b) is closed by means of coupling conditions. The first equation in (1c) below accounts for the linear poroelastic state law for the variations of the matrix porosity $\overline{\phi}_m$, with M denoting Biot's modulus. The second one stands for the

matrix–fracture transmission conditions for the Darcy flow model. Following [26, 45] they account for the normal flux continuity at each side $\mathfrak{a}$ of the fractures combined with a two-point approximation of the normal flux in the width of the fractures with Λ_f denoting the fracture normal transmissibility. The third equation in (1c) is the definition of the fracture aperture $\overline{d}_f$.

$$\begin{cases} \partial_t \overline{\phi}_m = b \ \mathrm{div}\, \partial_t \overline{\mathbf{u}} + \dfrac{1}{M} \partial_t \overline{p}_m & \text{on } (0,T) \times \Omega \backslash \overline{\Gamma}, \\ \overline{\mathbf{q}}_m \cdot \mathbf{n}^{\mathfrak{a}} = \Lambda_f [\![\overline{p}]\!]_{\mathfrak{a}} & \text{on } (0,T) \times \Gamma, \mathfrak{a} \in \{+,-\}, \\ \overline{d}_f = d_0 - [\![\overline{\mathbf{u}}]\!]_n & \text{on } (0,T) \times \Gamma. \end{cases} \tag{1c}$$

As shown in Figure 2, due to surface roughness, the fracture aperture $\overline{d}_f \geqslant d_0$ does not vanish except at the tips. The open space is always occupied by the fluid, which exerts on each side $\mathfrak{a}$ of the fracture the pressure $\overline{p}_f$ appearing in the definition of the contact traction $\overline{\mathbf{T}}^{\mathfrak{a}}$.

The strong formulation of the mixed-dimensional poromechanical model solves for the fluid pressures $\overline{p}_m, \overline{p}_f$ and the displacement field $\overline{\mathbf{u}}$, satisfying the mixed-dimensional Darcy flow model (1a) coupled to the contact mechanical model (1b) given the closure laws (1c). Let us refer to [11] for a weak formulation of this coupled model in the frictionless case. From the physical point of view, the fluid pressures act as a source term in the matrix and as a boundary condition along the fractures on the mechanical model, while the displacement field acts on the fluid flow via the porosity and fracture aperture changes throught the accumulation and conductivity terms (note that $\mathbb{K}_m$ can also depend on ϕ_m).

The following initial conditions are imposed on the pressures and matrix porosity

$$(\overline{p}_\omega)|_{t=0} = \overline{p}_{0,\omega}, \quad (\overline{\phi}_m)|_{t=0} = \overline{\phi}^0_m,$$

and normal flux conservation for $\overline{\mathbf{q}}_f$ is prescribed at fracture intersections not located on the boundary $\partial\Omega$.

Following [54] and [12], the quasi static poromechanical model with Coulomb frictional contact is formulated in mixed form using a vector Lagrange multiplier $\overline{\boldsymbol{\lambda}} : \Gamma \to \mathbb{R}^d$ at matrix–fracture interfaces. Denoting for $r \in \{1, d\}$ the duality pairing of $H^{-1/2}(\Gamma)^r$ and $H^{1/2}(\Gamma)^r$ by $\langle \cdot, \cdot \rangle_\Gamma$, we define the dual cone

$$\boldsymbol{\Lambda}(\overline{\lambda}_n) = \Big\{ \overline{\boldsymbol{\mu}} \in (H^{-1/2}(\Gamma))^d \ : \ \langle \overline{\boldsymbol{\mu}}, \overline{\mathbf{v}} \rangle_\Gamma \leqslant \langle F\overline{\lambda}_n, |\overline{\mathbf{v}}_\tau| \rangle_\Gamma \text{ for all } \overline{\mathbf{v}} \in (H^{1/2}(\Gamma))^d \text{ with } \overline{v}_n \leqslant 0 \Big\}.$$

The Lagrange multiplier formulation of (1b) then formally reads, dropping any consideration of regularity in time: find $\overline{\mathbf{u}} : [0,T] \to \mathbf{U}_0$ and $\overline{\boldsymbol{\lambda}} = (\overline{\lambda}_n, \overline{\boldsymbol{\lambda}}_\tau) : [0,T] \to \boldsymbol{\Lambda}(\overline{\lambda}_n)$ such that for all $\overline{\mathbf{v}} : [0,T] \to \mathbf{U}_0$ and $\overline{\boldsymbol{\mu}} = (\overline{\mu}_n, \overline{\boldsymbol{\mu}}_\tau) : [0,T] \to \boldsymbol{\Lambda}(\overline{\lambda}_n)$, one has

$$\begin{cases} \displaystyle\int_\Omega \Big(\boldsymbol{\sigma}(\overline{\mathbf{u}}) : \boldsymbol{\varepsilon}(\overline{\mathbf{v}}) - b\, \overline{p}_m \mathrm{div}(\overline{\mathbf{v}}) \Big) \mathrm{d}\mathbf{x} + \langle \overline{\boldsymbol{\lambda}}, [\![\overline{\mathbf{v}}]\!] \rangle_\Gamma + \int_\Gamma \overline{p}_f \ [\![\overline{\mathbf{v}}]\!]_n \ \mathrm{d}\sigma = \int_\Omega \mathbf{f} \cdot \overline{\mathbf{v}} \ \mathrm{d}\mathbf{x}, \\ \langle \overline{\mu}_n - \overline{\lambda}_n, [\![\overline{\mathbf{u}}]\!]_n \rangle_\Gamma + \langle \overline{\boldsymbol{\mu}}_\tau - \overline{\boldsymbol{\lambda}}_\tau, [\![\partial_t \overline{\mathbf{u}}]\!]_\tau \rangle_\Gamma \leqslant 0. \end{cases} \tag{2}$$

Note that, based on the variational formulation, the Lagrange multiplier satisfies $\overline{\boldsymbol{\lambda}} = -\mathbf{T}^+(\overline{\mathbf{u}}) = \mathbf{T}^-(\overline{\mathbf{u}})$. Note also that the Tresca friction model, frequently used to derive well-posedness and

error estimates, is obtained by freezing the slip threshold $-FT_n(\overline{\mathbf{u}})$ to a given non-negative function g. The mixed formulation (2) still applies provided that $F\overline{\lambda}_n$ is replaced by the fixed threshold g in the above definition of the dual cone.

3 Mixed, stabilized mixed and Nitsche's discretizations of the contact mechanical model

Let $\mathbf{U}_h$ denote a family of Finite Element subspaces of $\mathbf{U}_0$, indexed by h coming from a family of simplectic (to fix ideas) meshes $\mathcal{M}_h$ of the domain Ω. The mesh $\mathcal{M}_h$ is assumed conforming to the fracture network and we denote by $\mathcal{F}_\Gamma$ the subset of faces of the mesh such that

$$\overline{\Gamma} = \bigcup_{\sigma\in\mathcal{F}_\Gamma} \overline{\sigma}.$$

The family of meshes $\mathcal{M}_h$ is assumed to be shape regular in the sense that the shape regularity parameter $S_R = \max_h \max_{K\in\mathcal{M}_h} \frac{h_K}{\rho_K}$ is bounded, where h_K denotes the diameter of the cell K and ρ_K is the radius of the inscribed ball in K.

The subspace $M_h \subset L^2(\Gamma)$ denotes the set of piecewise constant functions on the partition $\mathcal{F}_\Gamma$ and we set $\mathbf{M}_h = (M_h)^d$. For $\boldsymbol{\lambda}$ in $\mathbf{M}_h$, we will still use the decomposition $\boldsymbol{\lambda} = (\lambda_n, \boldsymbol{\lambda}_\tau)$ with $\lambda_n = \boldsymbol{\lambda}\cdot\mathbf{n}^+$, $\boldsymbol{\lambda}_\tau = \boldsymbol{\lambda} - \lambda_n\mathbf{n}^+$, and identify $\boldsymbol{\lambda}_\tau$ to an element of $(M_h)^{d-1}$ based on an orthogonal basis local to each planar fracture. We denote by $\boldsymbol{\lambda}_\sigma$ the constant value of $\boldsymbol{\lambda} \in \mathbf{M}_h$ on the face $\sigma \in \mathcal{F}_\Gamma$ and by $\lambda_{n,\sigma}$ and $\boldsymbol{\lambda}_{\tau,\sigma}$ its normal and tangential components. The orthogonal projection from $L^2(\Gamma)$ to M_h is denoted by $\pi^0_{\mathcal{F}}$. By abuse of notations, the same notation will be used for the orthogonal projection from $(L^2(\Gamma))^d$ to $\mathbf{M}_h$. For a face $\sigma \in \mathcal{F}_\Gamma$, the face average projection will be denoted by π^0_σ in both cases.

After Euler implicit time integration and using an iterative coupling algorithm between the flow and the contact mechanical subproblems, we end up solving at each time step and each iterative coupling step the following static contact mechanical problem at given matrix and fracture pressures and previous time step displacement field $\overline{\mathbf{u}}^{n-1}$:

$$\begin{cases} -\mathrm{div}\Big(\boldsymbol{\sigma}(\overline{\mathbf{u}}) - b\,\overline{p}_m\mathbb{I}\Big) = \mathbf{f} & \text{in } \Omega\backslash\overline{\Gamma}, \\ \mathbf{T}^+(\overline{\mathbf{u}}) + \mathbf{T}^-(\overline{\mathbf{u}}) = \mathbf{0} & \text{in } \Gamma, \\ T_n(\overline{\mathbf{u}}) \leqslant 0,\ [\![\overline{\mathbf{u}}]\!]_n \leqslant 0,\ [\![\overline{\mathbf{u}}]\!]_n\, T_n(\overline{\mathbf{u}}) = 0 & \text{in } \Gamma, \\ |\mathbf{T}_\tau(\overline{\mathbf{u}})| \leqslant -F\ T_n(\overline{\mathbf{u}}) & \text{in } \Gamma, \\ ([\![\overline{\mathbf{u}} - \overline{\mathbf{u}}^{n-1}]\!]_\tau)\cdot\mathbf{T}_\tau(\overline{\mathbf{u}}) - F\ T_n(\overline{\mathbf{u}})|[\![\overline{\mathbf{u}} - \overline{\mathbf{u}}^{n-1}]\!]_\tau| = 0 & \text{in } \Gamma. \end{cases} \tag{3}$$

In what follows, we will set $\overline{\mathbf{u}}^{n-1} = 0$ for simplicity.

The following notations will be used. For all $x \in \mathbb{R}$, we set

$$[x]_{\mathbb{R}^-} = \min(0, x), \quad [x]_{\mathbb{R}^+} = \max(0, x) = -[-x]_{\mathbb{R}^-}.$$

For all $\mathbf{x} \in \mathbb{R}^{d-1}$ and $\alpha \geqslant 0$, we denote by $[\mathbf{x}]_\alpha$ the orthogonal projection of $\mathbf{x}$ on the ball $\mathcal{B}(\mathbf{0}, \alpha) \subset \mathbb{R}^{d-1}$ where $\mathcal{B}(\mathbf{0}, \alpha)$ is the closed ball of origin $\mathbf{0}$ and radius α, such that

$$[\mathbf{x}]_\alpha = \begin{cases} \mathbf{x} & \text{if } |\mathbf{x}| \leqslant \alpha, \\ \alpha\mathbf{x}/|\mathbf{x}| & \text{otherwise.} \end{cases}$$

3.1 Mixed discretization with facewise constant Lagrange multipliers

We focus in this work on mixed formulations based on facewise constant Lagrange multipliers which allows to readily deal with fracture intersections, corners and tips and leads to local expressions of the discrete contact conditions and efficient semi-smooth Newton solvers. On the other hand, they require to assume that the following uniform inf-sup condition between the space $\mathbf{U}_h$ of displacement fields and the space $\mathbf{M}_h$ of Lagrange multipliers is satisfied: there exists $c_\star$ independent on the mesh such that

$$\inf_{\boldsymbol{\mu}\in\mathbf{M}_h}\sup_{\mathbf{v}\in\mathbf{U}_h}\frac{\displaystyle\int_\Gamma \boldsymbol{\mu}\cdot[\![\mathbf{v}]\!]d\sigma}{\|\mathbf{v}\|_{\mathbf{U}_0}\|\boldsymbol{\mu}\|_{H^{-\frac{1}{2}}(\Gamma)^d}}\geqslant c_\star>0. \tag{4}$$

Let us define the discrete dual cone of normal Lagrange multipliers as

$$\Lambda_h=\{\lambda_n\in M_h\,|\,\lambda_n\geqslant 0 \text{ on } \Gamma\},$$

and the discrete dual cone of vectorial Lagrange multipliers given $\lambda_n\in\Lambda_h$ as

$$\boldsymbol{\Lambda}_h(\lambda_n)=\{\boldsymbol{\mu}=(\mu_n,\boldsymbol{\mu}_\tau)\in\mathbf{M}_h\,|\,\mu_n\geqslant 0,|\boldsymbol{\mu}_\tau|\leqslant F\lambda_n \text{ on } \Gamma\}.$$

Note that the friction coefficient will be assumed to be facewise constant on the partition $\mathcal{F}_\Gamma$.

The mixed discretization of the static contact mechanical model reads: find $(\mathbf{u},\boldsymbol{\lambda}=(\lambda_n,\boldsymbol{\lambda}_\tau))\in\mathbf{U}_h\times\boldsymbol{\Lambda}_h(\lambda_n)$ such that

$$\begin{cases}\displaystyle\int_\Omega\Big(\boldsymbol{\sigma}(\mathbf{u}):\boldsymbol{\varepsilon}(\mathbf{v})-b\,\overline{p}_m\mathrm{div}(\mathbf{v})\Big)\mathrm{d}\mathbf{x}+\int_\Gamma\boldsymbol{\lambda}\cdot[\![\mathbf{v}]\!]d\sigma+\int_\Gamma\overline{p}_f\,[\![\mathbf{v}]\!]_n\,\mathrm{d}\sigma=\int_\Omega\mathbf{f}\cdot\mathbf{v}\,\mathrm{d}\mathbf{x},\\[2ex]\displaystyle\int_\Gamma(\boldsymbol{\mu}-\boldsymbol{\lambda})\cdot[\![\mathbf{u}]\!]d\sigma\leqslant 0,\end{cases} \tag{5}$$

for all $(\mathbf{v},\boldsymbol{\mu})\in\mathbf{U}_h\times\boldsymbol{\Lambda}_h(\lambda_n)$. Note that the variational inequality in (5) is equivalent to the contact conditions between $\boldsymbol{\lambda}_\sigma$ and $\pi^0_\sigma[\![\mathbf{u}]\!]$ local to each face $\sigma\in\mathcal{F}_\Gamma$ (see e.g. Lemma 4.1 of [12]).

Let us denote by $P_{\boldsymbol{\Lambda}_h(\lambda_n)}$ the projection on the convex set $\boldsymbol{\Lambda}_h(\lambda_n)$. It is such that

$$P_{\boldsymbol{\Lambda}_h(\lambda_n)}\boldsymbol{\xi}=\Big([\xi_n]_{\mathbb{R}^+},[\boldsymbol{\xi}_\tau]_{\lambda_n}\Big), \tag{6}$$

for all $\boldsymbol{\xi}=(\xi_n,\boldsymbol{\xi}_\tau)\in\mathbf{M}_h$. Let us recall that $P_{\boldsymbol{\Lambda}_h(\lambda_n)}\boldsymbol{\xi}$ is the unique $\boldsymbol{\gamma}\in\boldsymbol{\Lambda}_h(\lambda_n)$ such that

$$\int_\Gamma(\boldsymbol{\mu}-\boldsymbol{\gamma})\cdot(\boldsymbol{\xi}-\boldsymbol{\gamma})d\sigma\leqslant 0 \text{ for all } \boldsymbol{\mu}\in\boldsymbol{\Lambda}_h(\lambda_n). \tag{7}$$

Then, noticing that the variational inequality in (5) is equivalent to $\boldsymbol{\lambda}\in\boldsymbol{\Lambda}_h(\lambda_n)$ such that

$$\int_\Gamma\Big[(\mu_n-\lambda_n)\Big(\beta_n^{\mathrm{sm}}\pi^0_{\mathcal{F}}[\![\mathbf{u}]\!]_n+\lambda_n-\lambda_n\Big)+(\boldsymbol{\mu}_\tau-\boldsymbol{\lambda}_\tau)\cdot\Big(\beta_\tau^{\mathrm{sm}}\pi^0_{\mathcal{F}}[\![\mathbf{u}]\!]_\tau+\boldsymbol{\lambda}_\tau-\boldsymbol{\lambda}_\tau\Big)\Big]d\sigma\leqslant 0,$$

for all $\boldsymbol{\mu} \in \boldsymbol{\Lambda}_h(\lambda_n)$ with constant (possibly facewise constant) parameters $\beta_n^{\rm sm} > 0$, $\beta_\tau^{\rm sm} > 0$, we deduce from (7) that

$$\boldsymbol{\lambda} = P_{\boldsymbol{\Lambda}_h(\lambda_n)}\Big(\beta_n^{\rm sm}\pi_{\mathcal{F}}^0[\![\mathbf{u}]\!]_n + \boldsymbol{\lambda}_n, \beta_\tau^{\rm sm}\pi_{\mathcal{F}}^0[\![\mathbf{u}]\!]_\tau + \boldsymbol{\lambda}_\tau\Big).$$

It results from (6) that the variational inequality in (5) is also equivalent to the following equations for each $\sigma \in \mathcal{F}_\Gamma$

$$\left\{\begin{array}{l} \lambda_{n,\sigma} - [\lambda_{n,\sigma} + \beta_n^{\rm sm}\pi_\sigma^0[\![\mathbf{u}]\!]_n]_{\mathbb{R}^+} = 0, \\ \boldsymbol{\lambda}_{\tau,\sigma} - [\boldsymbol{\lambda}_{\tau,\sigma} + \beta_\tau^{\rm sm}\pi_\sigma^0[\![\mathbf{u}]\!]_\tau]_{F_\sigma[\lambda_{n,\sigma}+\beta_n^{\rm sm}\pi_\sigma^0[\![\mathbf{u}]\!]_n]_{\mathbb{R}^+}} = 0, \end{array}\right. \tag{8}$$

which are the basis of the semi-smooth Newton algorithm used in the numerical section for the solution of the mixed discretization.

The well-posedness and convergence analysis of such mixed discretizations for frictionless contact is analysed in, e.g., [5, 37, 40, 55] (see also [38, 54] for Tresca friction). It readily extends to the case with pressure source terms.

3.2 Stabilized mixed discretization with facewise constant Lagrange multipliers and its equivalent Nitsche's formulation

In order to circumvent the inf-sup condition (4), we consider in this subsection the following stabilized mixed formulation in the spirit of [44, 41]. Exploiting their facewise constant approximation, the Lagrange multipliers can be eliminated leading to a Nitsche's type discretization with face averaging. It results that this stabilized mixed formulation can also be useful when $\mathbf{U}_h \times \mathbf{M}_h$ satisfies the inf-sup condition in order to eliminate the Lagrange multipliers. In that case, we will prove that the stabilized mixed solution converges to the mixed solution at the limit of large stabilization parameters.

3.2.1 Stabilized mixed discretization

Let us fix a parameter $\theta \in \mathbb{R}$ and two non-negative functions β_n and β_τ on Γ typically set to $\frac{\beta_n^0}{h_\sigma}$ and $\frac{\beta_\tau^0}{h_\sigma}$ on each face σ of Γ, where h_σ is the diameter of the face σ. By abuse of notations, in the following, h will also denote the facewise constant function of $L^2(\Gamma)$ with value h_σ on each face $\sigma \in \mathcal{F}_\Gamma$.

Let us introduce the following notations for the surface tractions with zero pressures

$$\left\{\begin{array}{l} \mathbf{T}^0(\overline{\mathbf{v}}) = \mathbb{\sigma}(\overline{\mathbf{v}})\mathbf{n}^+, \\ T_n^0(\overline{\mathbf{v}}) = \mathbf{T}^0(\overline{\mathbf{v}})\cdot\mathbf{n}^+, \\ \mathbf{T}_\tau^0(\overline{\mathbf{v}}) = \mathbf{T}^0(\overline{\mathbf{v}}) - (\mathbf{T}^0(\overline{\mathbf{v}})\cdot\mathbf{n}^+)\mathbf{n}^+. \end{array}\right.$$

The stabilized mixed discretization of the static contact mechanical model reads: find $(\mathbf{u}, \boldsymbol{\lambda} = (\lambda_n, \boldsymbol{\lambda}_\tau)) \in \mathbf{U}_h \times \boldsymbol{\Lambda}_h(\lambda_n)$ such that

$$\left\{\begin{array}{l} \displaystyle\int_\Omega \Big(\varpi(\mathbf{u}) : \mathfrak{e}(\mathbf{v}) - b\,\overline{p}_m \mathrm{div}(\mathbf{v})\Big)\mathrm{d}\mathbf{x} + \int_\Gamma \boldsymbol{\lambda}\cdot[\![\mathbf{v}]\!]d\sigma + \int_\Gamma \overline{p}_f\ [\![\mathbf{v}]\!]_n\ \mathrm{d}\sigma \\ \displaystyle -\int_\Gamma \frac{\theta}{\beta_n}(\lambda_n + T_n(\mathbf{u}))\pi^0_{\mathcal{F}} T^0_n(\mathbf{v})d\sigma - \int_\Gamma \frac{\theta}{\beta_\tau}(\boldsymbol{\lambda}_\tau + \mathbf{T}_\tau(\mathbf{u}))\cdot \pi^0_{\mathcal{F}}\mathbf{T}^0_\tau(\mathbf{v})d\sigma = \int_\Omega \mathbf{f}\cdot\mathbf{v}\ \mathrm{d}\mathbf{x}, \\ \displaystyle\int_\Gamma (\boldsymbol{\mu}-\boldsymbol{\lambda})\cdot[\![\mathbf{u}]\!]d\sigma \\ \displaystyle -\int_\Gamma \frac{1}{\beta_n}(\mu_n-\lambda_n)(\lambda_n + T_n(\mathbf{u}))d\sigma - \int_\Gamma \frac{1}{\beta_\tau}(\boldsymbol{\mu}_\tau-\boldsymbol{\lambda}_\tau)\cdot(\boldsymbol{\lambda}_\tau + \mathbf{T}_\tau(\mathbf{u}))d\sigma \leqslant 0, \end{array}\right. \tag{9}$$

for all $(\mathbf{v},\boldsymbol{\mu}) \in \mathbf{U}_h \times \boldsymbol{\Lambda}_h(\lambda_n)$.

3.2.2 Equivalent Nitsche's formulation

The following Proposition states that, thanks to their facewise constant approximations, the Lagrange multipliers can be eliminated from the stabilized mixed formulation.

Proposition 3.1. *The variational inequality in (9) with $\boldsymbol{\lambda} \in \boldsymbol{\Lambda}_h(\lambda_n)$ is equivalent to the following equations:*

$$\left\{\begin{array}{rcl} -\lambda_n & = & [\pi^0_{\mathcal{F}}\Big(T_n(\mathbf{u}) - \beta_n[\![\mathbf{u}]\!]_n\Big)]_{\mathbb{R}^-}, \\ -\boldsymbol{\lambda}_\tau & = & [\pi^0_{\mathcal{F}}\Big(\mathbf{T}_\tau(\mathbf{u}) - \beta_\tau[\![\mathbf{u}]\!]_\tau\Big)]\Big(-F\Big[\pi^0_{\mathcal{F}}\Big(T_n(\mathbf{u})-\beta_n[\![\mathbf{u}]\!]_n\Big)\Big]_{\mathbb{R}^-}\Big). \end{array}\right. \tag{10}$$

Proof. The inequality in (9) is equivalent to

$$\int_\Gamma \Big[(\mu_n-\lambda_n)\Big(-\pi^0_{\mathcal{F}}(T_n(\mathbf{u})-\beta_n[\![\mathbf{u}]\!]_n)-\lambda_n\Big) + (\boldsymbol{\mu}_\tau-\boldsymbol{\lambda}_\tau)\cdot\Big(-\pi^0_{\mathcal{F}}(\mathbf{T}_\tau(\mathbf{u})-\beta_\tau[\![\mathbf{u}]\!]_\tau)-\boldsymbol{\lambda}_\tau\Big)\Big]d\sigma \leqslant 0.$$

We deduce from (7) that the variational inequality in (9) is equivalent to

$$\boldsymbol{\lambda} = P_{\boldsymbol{\Lambda}_h(\lambda_n)}\Big(-\pi^0_{\mathcal{F}}(T_n(\mathbf{u}) - \beta_n[\![\mathbf{u}]\!]_n), -\pi^0_{\mathcal{F}}(\mathbf{T}_\tau(\mathbf{u}) - \beta_\tau[\![\mathbf{u}]\!]_\tau)\Big),$$

concluding the proof from (6). □

From (10), we can eliminate the Lagrange multipliers leading to the following equivalent Nitsche's type formulation: find $\mathbf{u} \in \mathbf{U}_h$ such that

$$
\begin{aligned}
&\int_\Omega \Big(\boldsymbol{\sigma}(\mathbf{u}) : \mathfrak{e}(\mathbf{v}) - b\,\overline{p}_m \mathrm{div}(\mathbf{v})\Big)\mathrm{d}\mathbf{x} + \int_\Gamma \overline{p}_f\ [\![\mathbf{v}]\!]_n\ \mathrm{d}\sigma \\
&- \int_\Gamma \frac{\theta}{\beta_n} T_n(\mathbf{u}) \cdot \pi_{\mathcal{F}}^0 T_n^0(\mathbf{v})\ \mathrm{d}\sigma - \int_\Gamma \frac{\theta}{\beta_\tau} \mathbf{T}_\tau(\mathbf{u}) \cdot \pi_{\mathcal{F}}^0 \mathbf{T}_\tau^0(\mathbf{v})\ \mathrm{d}\sigma \\
&+ \int_\Gamma \frac{1}{\beta_n} \Big[\pi_{\mathcal{F}}^0\Big(T_n(\mathbf{u}) - \beta_n [\![\mathbf{u}]\!]_n\Big)\Big]_{\mathbb{R}^-} \Big(\theta T_n^0(\mathbf{v}) - \beta_n [\![\mathbf{v}]\!]_n\Big)\ \mathrm{d}\sigma \\
&+ \int_\Gamma \frac{1}{\beta_\tau} \Big[\pi_{\mathcal{F}}^0\Big(\mathbf{T}_\tau(\mathbf{u}) - \beta_\tau [\![\mathbf{u}]\!]_\tau\Big)\Big]_{\Big(-F\Big[\pi_{\mathcal{F}}^0\Big(T_n(\mathbf{u}) - \beta_n [\![\mathbf{u}]\!]_n\Big)\Big]_{\mathbb{R}^-}\Big)} \cdot \Big(\theta \mathbf{T}_\tau^0(\mathbf{v}) - \beta_\tau [\![\mathbf{v}]\!]_\tau\Big)\ \mathrm{d}\sigma \\
&= \int_\Omega \mathbf{f} \cdot \mathbf{v}\ \mathrm{d}\mathbf{x},
\end{aligned}
\tag{11}
$$

for all $\mathbf{v} \in \mathbf{U}_h$. Due to the face averaging, this formulation will be termed mean-Nitsche's method in the following. Note that it is not consistent in the usual Nitsche's sense since the exact solution $\overline{\mathbf{u}}$ does not satisfy (11). It is only consistent as a mixed formulation in the sense that $(\overline{\mathbf{u}}, \overline{\boldsymbol{\lambda}})$ satisfies (9).

Let us consider the Tresca friction model obtained by freezing the slip threshold $-FT_n(\overline{\mathbf{u}})$ to a given non-negative function g. The stabilized mixed and mixed discretisations of the Tresca model are obtained by replacing $\boldsymbol{\Lambda}_h(\lambda_n)$ by $\boldsymbol{\Lambda}_h(\pi_{\mathcal{F}}^0 g)$ and the mean-Nitsche's formulation is derived by replacing $-F\Big[\pi_{\mathcal{F}}^0\Big(T_n(\mathbf{u}) - \beta_n [\![\mathbf{u}]\!]_n\Big)\Big]_{\mathbb{R}^-}$ by $\pi_{\mathcal{F}}^0 g$ in (11).

The well-posedness analysis of the mean-Nitsche's formulation is similar to the one for the Nitsche's discretization from [20] for the Tresca model. It results that the stabilized mixed method is also well-posed for the Tresca model. For the Coulomb frictional model, an existence result can also be derived for the mean-Nitsche's formulation (and stabilized mixed method) following [23].

An a priori error estimate can be derived starting from the stabilized mixed formulation for the Tresca friction model. Assuming the inf-sup condition to hold, this estimate is robust in the limit of large penalization parameters β_n^0 and β_τ^0 as opposed to what is achieved in the general case for the stabilized mixed discretization [41] and the Nitsche's method [20].

Proposition 3.2. *Let us set $\beta^0 = \beta_n^0 = \beta_\tau^0$ for the sake of simplicity. Let us assume that the Tresca threshold g is constant and that the unique solution $(\overline{\mathbf{u}}, \overline{\boldsymbol{\lambda}})$ of (2) for the static contact mechanical model with Tresca friction is in $H^{3/2+\nu}(\Omega\backslash\overline{\Gamma})^d \times H^\nu(\Gamma)^d$. Then, the following a priori error estimate holds for the unique solution $(\mathbf{u}, \boldsymbol{\lambda}) \in \mathbf{U}_h \times \boldsymbol{\Lambda}_h(g)$ of (9) assuming that the Nitsche's parameter β^0 is large enough:*

$$
\|\overline{\mathbf{u}} - \mathbf{u}\|_{\mathbf{U}_0} + c\|h^{1/2}(\overline{\boldsymbol{\lambda}} - \boldsymbol{\lambda})\|_{L^2(\Gamma)^d} \leqslant C h^{1/2+\nu/2}\Big(\|\overline{\mathbf{u}}\|_{H^{3/2+\nu}(\Omega\backslash\overline{\Gamma})^d} + \|\overline{\boldsymbol{\lambda}}\|_{H^\nu(\Gamma)^d}\Big),
\tag{12}
$$

with $c = \frac{1}{\beta^0}$, $0 < \nu \leqslant \min(1, k - 1/2)$ where k is the degree of approximation of $\mathbf{U}_h$, and C is a constant independent on h, $\overline{\mathbf{u}}$ and $\overline{\boldsymbol{\lambda}}$ but depending on β^0 and on the shape regularity parameter S_R. Furthermore, if the inf-sup condition (4) holds, we can take $c = 1$ and the constant C is independent on (still large enough) β^0.

Proof. In the general case, the proof of the a priori error estimate is a simple adaptation to the Tresca friction model of the analysis carried out in [41] for the frictionless model. The degeneracy of the error estimate for large values of the penalization parameters stems from the estimation of the term

$$\int_\Gamma (\overline{\boldsymbol{\lambda}} - \boldsymbol{\lambda}) \cdot ([\![\overline{\mathbf{u}}]\!] - [\![I_h \overline{\mathbf{u}}]\!]) d\sigma, \tag{13}$$

where I_h is the Lagrange interpolation operator onto $\mathbf{U}_h$. In [41], (13) is estimated from the Young inequality as

$$\int_\Gamma (\overline{\boldsymbol{\lambda}} - \boldsymbol{\lambda}) \cdot ([\![\overline{\mathbf{u}}]\!] - [\![I_h \overline{\mathbf{u}}]\!]) d\sigma \leqslant \alpha \frac{1}{\beta^0} \|h^{1/2}(\overline{\boldsymbol{\lambda}} - \boldsymbol{\lambda})\|^2_{L^2(\Gamma)^d} + \frac{1}{4\alpha} \beta^0 \|h^{-1/2}([\![\overline{\mathbf{u}}]\!] - [\![I_h \overline{\mathbf{u}}]\!])\|^2_{L^2(\Gamma)^d},$$

for all $\alpha > 0$ providing the non-robust term $\beta^0 \|h^{-1/2}([\![\overline{\mathbf{u}}]\!] - [\![I_h \overline{\mathbf{u}}]\!])\|^2_{L^2(\Gamma)^d}$ which is responsible for the dependence of C on β^0 in (12).

This can be fixed from the inf-sup condition (4). To show this, let us substract the variational equalities (2) and (9) with test function $\mathbf{v} \in \mathbf{U}_h$. Taking into account that $\overline{\boldsymbol{\lambda}} = -\mathbf{T}(\overline{\mathbf{u}})$, we obtain

$$\int_\Gamma (\overline{\boldsymbol{\lambda}} - \boldsymbol{\lambda}) \cdot [\![\mathbf{v}]\!] d\sigma = -\int_\Omega \boldsymbol{\sigma}(\overline{\mathbf{u}} - \mathbf{u}) : \mathbb{c}(\mathbf{v}) d\mathbf{x} + \int_\Gamma \frac{\theta}{\beta_n} (\overline{\boldsymbol{\lambda}} - \boldsymbol{\lambda} + \mathbf{T}^0(\overline{\mathbf{u}} - \mathbf{u})) \cdot \pi^0_{\mathcal{F}} \mathbf{T}^0(\mathbf{v}) d\sigma.$$

Let C denote in the following a generic constant independent on h and β^0. Using that $\|h^{1/2}\mathbf{T}^0(\mathbf{v})\|_{L^2(\Gamma)^d} \leqslant C\|\mathbf{v}\|_{\mathbf{U}_0}$ for all $\mathbf{v} \in \mathbf{U}_h$ (see Lemma 3.2 of [20]), we deduce that

$$\sup_{\mathbf{v} \in \mathbf{U}_h} \frac{\displaystyle\int_\Gamma (\overline{\boldsymbol{\lambda}} - \boldsymbol{\lambda}) \cdot [\![\mathbf{v}]\!] d\sigma}{\|\mathbf{v}\|_{\mathbf{U}_0}} \leqslant C\Big(\|\overline{\mathbf{u}} - \mathbf{u}\|_{\mathbf{U}_0} + \frac{1}{\beta^0} \|h^{1/2}(\overline{\boldsymbol{\lambda}} - \boldsymbol{\lambda})\|_{L^2(\Gamma)^d} + \frac{1}{\beta^0} \|h^{1/2}\mathbf{T}^0(\overline{\mathbf{u}} - \mathbf{u})\|_{L^2(\Gamma)^d} \Big). \tag{14}$$

Using the bound $\|h^{1/2}\boldsymbol{\mu}\|_{L^2(\Gamma)^d} \leqslant C\|\boldsymbol{\mu}\|_{H^{-1/2}(\Gamma)^d}$ for all $\boldsymbol{\mu} \in \mathbf{M}_h$, and the inf-sup condition (4), we obtain the estimate

$$\begin{aligned} \|h^{1/2}(\boldsymbol{\mu} - \boldsymbol{\lambda})\|_{L^2(\Gamma)^d} &\leqslant C\|\boldsymbol{\mu} - \boldsymbol{\lambda}\|_{H^{-1/2}(\Gamma)^d} \leqslant C \sup_{\mathbf{v} \in \mathbf{U}_h} \frac{\displaystyle\int_\Gamma (\boldsymbol{\mu} - \overline{\boldsymbol{\lambda}} + \overline{\boldsymbol{\lambda}} - \boldsymbol{\lambda}) \cdot [\![\mathbf{v}]\!] d\sigma}{\|\mathbf{v}\|_{\mathbf{U}_0}}, \\ &\leqslant C\Big(\|\boldsymbol{\mu} - \overline{\boldsymbol{\lambda}}\|_{H^{-1/2}(\Gamma)^d} + \sup_{\mathbf{v} \in \mathbf{U}_h} \frac{\displaystyle\int_\Gamma (\overline{\boldsymbol{\lambda}} - \boldsymbol{\lambda}) \cdot [\![\mathbf{v}]\!] d\sigma}{\|\mathbf{v}\|_{\mathbf{U}_0}} \Big). \end{aligned}$$

It results that

$$\|h^{1/2}(\overline{\boldsymbol{\lambda}} - \boldsymbol{\lambda})\|_{L^2(\Gamma)^d} \leqslant C\Big(\|\boldsymbol{\mu} - \overline{\boldsymbol{\lambda}}\|_{H^{-1/2}(\Gamma)^d} + \|h^{1/2}(\boldsymbol{\mu} - \overline{\boldsymbol{\lambda}})\|_{L^2(\Gamma)^d} + \sup_{\mathbf{v} \in \mathbf{U}_h} \frac{\displaystyle\int_\Gamma (\overline{\boldsymbol{\lambda}} - \boldsymbol{\lambda}) \cdot [\![\mathbf{v}]\!] d\sigma}{\|\mathbf{v}\|_{\mathbf{U}_0}} \Big). \tag{15}$$

Combining (15) with (14) we obtain that the following abstract estimate holds for large enough β^0:

$$\|h^{1/2}(\overline{\boldsymbol{\lambda}} - \boldsymbol{\lambda})\|_{L^2(\Gamma)^d} \leqslant C\Big[\|\overline{\mathbf{u}} - \mathbf{u}\|_{\mathbf{U}_0} + \inf_{\boldsymbol{\mu} \in \mathbf{M}_h} \Big(\|\boldsymbol{\mu} - \overline{\boldsymbol{\lambda}}\|_{H^{-1/2}(\Gamma)^d} + \|h^{1/2}(\boldsymbol{\mu} - \overline{\boldsymbol{\lambda}})\|_{L^2(\Gamma)^d} \Big)$$

$$+ \inf_{\mathbf{v}\in\mathbf{U}_h}\Big(\|\overline{\mathbf{u}}-\mathbf{v}\|_{\mathbf{U}_0}+\|h^{1/2}\mathbf{T}^0(\overline{\mathbf{u}}-\mathbf{v})\|_{L^2(\Gamma)^d}\Big).$$

Setting $\mathbf{v}=I_h\overline{\mathbf{u}}$ and $\boldsymbol{\mu}=\pi^0_{\mathcal{F}}\overline{\boldsymbol{\lambda}}$, we obtain the estimate

$$\|h^{1/2}(\overline{\boldsymbol{\lambda}}-\boldsymbol{\lambda})\|_{L^2(\Gamma)^d}\leqslant C\Big(\|\overline{\mathbf{u}}-\mathbf{u}\|_{\mathbf{U}_0}+h^{1/2+\nu}(\|\overline{\mathbf{u}}\|_{H^{3/2+\nu}(\Omega\setminus\overline{\Gamma})^d}+\|\overline{\boldsymbol{\lambda}}\|_{H^{\nu}(\Gamma)^d})\Big),$$

with $0<\nu\leqslant\min(1,k-1/2)$. Using

$$\|h^{-1/2}([\![\overline{\mathbf{u}}]\!]-[\![I_h\overline{\mathbf{u}}]\!])\|_{L^2(\Gamma)^d}\leqslant Ch^{1/2+\nu}\|\overline{\mathbf{u}}\|_{H^{3/2+\nu}(\Omega\setminus\overline{\Gamma})^d},$$

and the Young inequality, we deduce that, for all $\alpha>0$, we have the estimate

$$\int_\Gamma(\overline{\boldsymbol{\lambda}}-\boldsymbol{\lambda})\cdot([\![\overline{\mathbf{u}}]\!]-[\![I_h\overline{\mathbf{u}}]\!])d\sigma\leqslant\alpha\|\overline{\mathbf{u}}-\mathbf{u}\|^2_{\mathbf{U}_0}+C(\frac{1}{\alpha}+1)h^{1+2\nu}(\|\overline{\mathbf{u}}\|^2_{H^{3/2+\nu}(\Omega\setminus\overline{\Gamma})^d}+\|\overline{\boldsymbol{\lambda}}\|^2_{H^{\nu}(\Gamma)^d})\Big),$$

which, combined with the analysis in [41], yields a robust error estimate w.r.t. large enough β^0.

□

3.2.3 Convergence to the mixed solution

The following proposition states a first order error estimate in $\frac{1}{\beta^0}$ between the discrete solutions of the stabilized mixed (9) and mixed (5) discretizations of the Tresca friction model.

Proposition 3.3. *Let us set $\beta^0=\min(\beta^0_n,\beta^0_\tau)$ assumed to be large enough. Let us denote respectively by $(\mathbf{u}_\beta,\boldsymbol{\lambda}_\beta)\in\mathbf{U}_h\times\boldsymbol{\Lambda}_h(\pi^0_{\mathcal{F}}g)$ and $(\mathbf{u},\boldsymbol{\lambda})\in\mathbf{U}_h\times\boldsymbol{\Lambda}_h(\pi^0_{\mathcal{F}}g)$ the unique solutions of the stabilized mixed (9) and mixed (5) discretizations of the Tresca friction model. Assuming the inf-sup condition (4) to hold, we have the following error estimates:*

$$\|\mathbf{u}-\mathbf{u}_\beta\|_{\mathbf{U}_0}+\|h^{1/2}(\boldsymbol{\lambda}-\boldsymbol{\lambda}_\beta)\|_{L^2(\Gamma)^d}\leqslant\frac{C}{\beta^0},\tag{16}$$

with C independent of h and β^0_n, β^0_τ but depending on the shape regularity parameter S_R and the physical data.

Proof. We denote by C a generic non-negative constant independent on β^0_n, β^0_τ and h but possibly depending on the shape regularity parameter S_R and the physical data. The well-posedness of the stabilized mixed discretization (9) can be derived from its equivalent mean-Nitsche's formulation (11) using the same techniques as in [20]. It results that for β^0 large enough, there exists a unique solution $\mathbf{u}_\beta\in\mathbf{U}_h$ to (11) and a constant C such that

$$\|\mathbf{u}_\beta\|_{\mathbf{U}_0}\leqslant C.\tag{17}$$

Using the inf-sup assumption (4), the bound $\|h^{1/2}\boldsymbol{\mu}\|_{L^2(\Gamma)^d}\leqslant C\|\boldsymbol{\mu}\|_{H^{-1/2}(\Gamma)^d}$ for all $\boldsymbol{\mu}\in\mathbf{M}_h$, and the variational equality in (9), we obtain that

$$\|h^{1/2}\boldsymbol{\lambda}_\beta\|_{L^2(\Gamma)^d}\leqslant C\sup_{\mathbf{v}\in\mathbf{U}_h}\frac{1}{\|\mathbf{v}\|_{\mathbf{U}_0}}\Big[-\int_\Omega\Big(\boldsymbol{\sigma}(\mathbf{u}_\beta):\boldsymbol{\varepsilon}(\mathbf{v})-b\,\overline{p}_m\mathrm{div}(\mathbf{v})\Big)\mathrm{d}\mathbf{x}-\int_\Gamma\overline{p}_f\,[\![\mathbf{v}]\!]_n\,\mathrm{d}\sigma$$

$$+\int_\Gamma \frac{\theta}{\beta_n}(\lambda_{\beta,n}+T_n(\mathbf{u}_\beta))\pi^0_{\mathcal{F}}T^0_n(\mathbf{v})d\sigma+\int_\Gamma \frac{\theta}{\beta_\tau}(\boldsymbol{\lambda}_{\beta,\tau}+\mathbf{T}_\tau(\mathbf{u}_\beta))\cdot\pi^0_{\mathcal{F}}\mathbf{T}^0_\tau(\mathbf{v})d\sigma+\int_\Omega \mathbf{f}\cdot\mathbf{v}\ \mathrm{d}\mathbf{x}\Big].$$

Then, using that $\|h^{1/2}\mathbf{T}^0(\mathbf{v})\|_{L^2(\Gamma)^d}\leqslant C\|\mathbf{v}\|_{\mathbf{U}_0}$ for all $\mathbf{v}\in\mathbf{U}_h$, we obtain the estimate

$$\|h^{1/2}\boldsymbol{\lambda}_\beta\|_{L^2(\Gamma)^d}\leqslant C\Big(1+\|\mathbf{u}_\beta\|_{\mathbf{U}_0}+\frac{1}{\beta^0}\|h^{1/2}\boldsymbol{\lambda}_\beta\|_{L^2(\Gamma)^d}\Big).$$

It results that for β^0 large enough, we have

$$\|h^{1/2}\boldsymbol{\lambda}_\beta\|_{L^2(\Gamma)^d}\leqslant C. \tag{18}$$

Taking the difference between the variational equalities in (9) and (5), we obtain that

$$\begin{aligned}&\int_\Omega\Big(\boldsymbol{\sigma}(\mathbf{u}_\beta-\mathbf{u}):\boldsymbol{\varepsilon}(\mathbf{v})+\int_\Gamma(\boldsymbol{\lambda}_\beta-\boldsymbol{\lambda})\cdot[\![\mathbf{v}]\!]d\sigma\\&-\int_\Gamma\frac{\theta}{\beta_n}(\lambda_{\beta,n}+T_n(\mathbf{u}_\beta))\pi^0_{\mathcal{F}}T^0_n(\mathbf{v})-\int_\Gamma\frac{\theta}{\beta_\tau}(\boldsymbol{\lambda}_{\beta,\tau}+\mathbf{T}_\tau(\mathbf{u}_\beta))\cdot\pi^0_{\mathcal{F}}\mathbf{T}^0_\tau(\mathbf{v})=0.\end{aligned} \tag{19}$$

Setting $\mathbf{v}=\mathbf{u}_\beta-\mathbf{u}$ in (19), using the bounds (18), (17), $\|h^{1/2}\mathbf{T}^0(\mathbf{u}_\beta)\|_{L^2(\Gamma)^d}\leqslant C\|\mathbf{u}_\beta\|_{\mathbf{U}_0}$ and $\|h^{1/2}\pi^0_{\mathcal{F}}\mathbf{T}^0(\mathbf{v})\|_{L^2(\Gamma)^d}\leqslant C\|\mathbf{v}\|_{\mathbf{U}_0}$, we obtain the estimate

$$\|\mathbf{u}_\beta-\mathbf{u}\|^2_{\mathbf{U}_0}\leqslant C\Big(\int_\Gamma(\boldsymbol{\lambda}-\boldsymbol{\lambda}_\beta)\cdot([\![\mathbf{u}_\beta]\!]-[\![\mathbf{u}]\!])d\sigma+\frac{1}{\beta_0}\|\mathbf{u}_\beta-\mathbf{u}\|_{\mathbf{U}_0}\Big). \tag{20}$$

Let us set $\boldsymbol{\mu}=\boldsymbol{\lambda}$ in the variational inequality of (9). From the bound $\|h^{1/2}(\boldsymbol{\lambda}_\beta+\mathbf{T}(\mathbf{u}_\beta))\|_{L^2(\Gamma)^d}\leqslant C$, we obtain the inequality

$$\int_\Gamma(\boldsymbol{\lambda}-\boldsymbol{\lambda}_\beta)\cdot[\![\mathbf{u}_\beta]\!]d\sigma\leqslant\frac{C}{\beta^0}\|h^{1/2}(\boldsymbol{\lambda}-\boldsymbol{\lambda}_\beta)\|_{L^2(\Gamma)^d}.$$

Combining this inequality with the variational inequality of (5) for $\boldsymbol{\mu}=\boldsymbol{\lambda}_\beta$, we obtain the estimate

$$\int_\Gamma(\boldsymbol{\lambda}-\boldsymbol{\lambda}_\beta)\cdot([\![\mathbf{u}_\beta]\!]-[\![\mathbf{u}]\!])d\sigma\leqslant\frac{C}{\beta^0}\|h^{1/2}(\boldsymbol{\lambda}-\boldsymbol{\lambda}_\beta)\|_{L^2(\Gamma)^d}. \tag{21}$$

Combining the estimates (20) and (21), we get that

$$\|\mathbf{u}_\beta-\mathbf{u}\|^2_{\mathbf{U}_0}\leqslant\frac{C}{\beta^0}\Big(\|\mathbf{u}_\beta-\mathbf{u}\|_{\mathbf{U}_0}+\|h^{1/2}(\boldsymbol{\lambda}-\boldsymbol{\lambda}_\beta)\|_{L^2(\Gamma)^d}\Big). \tag{22}$$

From the inf-sup condition (4) and (19), we get the estimate

$$\|h^{1/2}(\boldsymbol{\lambda}-\boldsymbol{\lambda}_\beta)\|_{L^2(\Gamma)^d}\leqslant C\Big(\|\mathbf{u}_\beta-\mathbf{u}\|_{\mathbf{U}_0}+\frac{1}{\beta^0}\Big). \tag{23}$$

Combining the estimates (22) and (23) with the Young inequality concludes the proof of (16). □

For the Coulomb frictional model we can state the following Proposition.

Proposition 3.4. *Let $\overline{\beta}^0 > 0$ be large enough. For $\beta^0 \geqslant \overline{\beta}^0$, there exists a solution $(\mathbf{u}_\beta, \boldsymbol{\lambda}_\beta) \in \mathbf{U}_h \times \boldsymbol{\Lambda}_h(\lambda_{\beta,n})$ to (9) with $\|\mathbf{u}_\beta\|_{\mathbf{U}_0} + \|h^{1/2}\boldsymbol{\lambda}_\beta\|_{L^2(\Gamma)^d} \leqslant C$, C independent of β_n^0, β_τ^0 and h but depending on the shape regularity parameter S_R and the physical data. Furthermore, any sequence of such solutions with β^0 going to infinity admits a subsequence which converges to $(\mathbf{u}, \boldsymbol{\lambda}) \in \mathbf{U}_h \times \boldsymbol{\Lambda}_h(\lambda_n)$ solution of (5).*

Proof. The existence of a solution to the mean-Nitsche's formulation (11) can be established as in [23] for β^0 large enough using the Brouwer fixed point theorem based on the Tresca friction solution. By construction the solution is bounded in the sense that there exists C independent of β_n^0, β_τ^0 and h but depending on the shape regularity parameter S_R and the physical data such that $\|\mathbf{u}_\beta\|_{\mathbf{U}_0} \leqslant C$. Then, the bound on the Lagrange multiplier $\|h^{1/2}\boldsymbol{\lambda}_\beta\|_{L^2(\Gamma)^d} \leqslant C$ follows as in the previous proof from the inf-sup assumption and for β^0 large enough. For any sequence of such solutions with $\beta^0 \to +\infty$, we can extract a subsequence which converges to $(\mathbf{u}, \boldsymbol{\lambda}) \in \mathbf{U}_h \times \mathbf{M}_h$. From (10), we have

$$\left\{\begin{array}{rcl} \lambda_n & = & -\lim\limits_{\beta^0\to+\infty}[\pi_{\mathcal{F}}^0\Big(T_n(\mathbf{u}_\beta) - \beta_n[\![\mathbf{u}_\beta]\!]_n\Big)]_{\mathbb{R}^-}, \\ \boldsymbol{\lambda}_\tau & = & -\lim\limits_{\beta^0\to+\infty}[\pi_{\mathcal{F}}^0\Big(\mathbf{T}_\tau(\mathbf{u}_\beta) - \beta_\tau[\![\mathbf{u}_\beta]\!]_\tau\Big)]\Big(-F\Big[\pi_{\mathcal{F}}^0\Big(T_n(\mathbf{u}_\beta)-\beta_n[\![\mathbf{u}_\beta]\!]_n\Big)\Big]_{\mathbb{R}^-}\Big) \end{array}\right.$$

from which we deduce that $\boldsymbol{\lambda} \in \boldsymbol{\Lambda}_h(\lambda_n)$. Let $\boldsymbol{\mu} = (\mu_n, \boldsymbol{\mu}_\tau) \in \boldsymbol{\Lambda}_h(\lambda_n)$. The sequence $\boldsymbol{\mu}_\beta = (\mu_{\beta,n}, \boldsymbol{\mu}_{\beta,\tau}) \in \boldsymbol{\Lambda}_h(\lambda_{\beta,n})$ such that

$$\boldsymbol{\mu}_{\beta,\sigma} = \left\{\begin{array}{l} (\mu_{n,\sigma}, \boldsymbol{\mu}_{\tau,\sigma} = 0) \text{ if } F_\sigma\lambda_{n,\sigma} = 0, \\ (\mu_{n,\sigma}, \dfrac{\boldsymbol{\mu}_{\tau,\sigma}}{F_\sigma\lambda_{n,\sigma}} F_\sigma\lambda_{\beta,n,\sigma}) \text{ else,} \end{array}\right.$$

converges to $\boldsymbol{\mu}$. Then, passing to the limit in the stabilized mixed variational formulation (9) with $(\mathbf{v}, \boldsymbol{\mu}_\beta)$ as test functions shows that $(\mathbf{u}, \boldsymbol{\lambda})$ satisfies the mixed formulation (5) which concludes the proof. □

3.3 Nitsche's discretization

We follow the Nitsche's formulation introduced in [20] for Tresca and in [23] for Coulomb frictional models. It can be obtained by dropping the face averaging operators in (11): find $\mathbf{u} \in \mathbf{U}_h$ such that for all $\mathbf{v} \in \mathbf{U}_h$, one has

$$\begin{aligned} &\int_\Omega \Big(\boldsymbol{\sigma}(\mathbf{u}) : \mathfrak{e}(\mathbf{v}) - b\,\overline{p}_m \mathrm{div}(\mathbf{v})\Big)\mathrm{d}\mathbf{x} + \int_\Gamma \overline{p}_f\ [\![\mathbf{v}]\!]_n\ \mathrm{d}\sigma \\ &- \int_\Gamma \frac{\theta}{\beta_n} T_n(\mathbf{u}) \cdot T_n^0(\mathbf{v})\ \mathrm{d}\sigma - \int_\Gamma \frac{\theta}{\beta_\tau} \mathbf{T}_\tau(\mathbf{u}) \cdot \mathbf{T}_\tau^0(\mathbf{v})\ \mathrm{d}\sigma \\ &+ \int_\Gamma \frac{1}{\beta_n}\Big[T_n(\mathbf{u}) - \beta_n[\![\mathbf{u}]\!]_n\Big]_{\mathbb{R}^-}\Big(\theta T_n^0(\mathbf{v}) - \beta_n[\![\mathbf{v}]\!]_n\Big)\ \mathrm{d}\sigma \\ &+ \int_\Gamma \frac{1}{\beta_\tau}\Big[\mathbf{T}_\tau(\mathbf{u}) - \beta_\tau[\![\mathbf{u}]\!]_\tau\Big]_{\Big(-F\Big[T_n(\mathbf{u})-\beta_n[\![\mathbf{u}]\!]_n\Big]_{\mathbb{R}^-}\Big)} \cdot \Big(\theta\mathbf{T}_\tau^0(\mathbf{v}) - \beta_\tau[\![\mathbf{v}]\!]_\tau\Big)\ \mathrm{d}\sigma \\ &= \int_\Omega \mathbf{f} \cdot \mathbf{v}\ \mathrm{d}\mathbf{x}, \end{aligned} \tag{24}$$

The well-posedness of (24) for the Tresca friction model is shown in [20] to hold for Nitsche's parameters such that

$$(1+\theta)^2\left(\frac{\gamma_n}{\beta_n^0}+\frac{\gamma_\tau}{\beta_\tau^0}\right)\leqslant C, \tag{25}$$

for any given $C<4$ with

$$\gamma_n=\sup_{\mathbf{v}\in\mathbf{U}_h}\frac{\|h^{\frac{1}{2}}T_n^0(\mathbf{v})\|^2_{L^2(\Gamma)}}{\displaystyle\int_\Omega \boldsymbol{\sigma}(\mathbf{v}):\boldsymbol{\varepsilon}(\mathbf{v})d\mathbf{x}},\quad \gamma_\tau=\sup_{\mathbf{v}\in\mathbf{U}_h}\frac{\|h^{\frac{1}{2}}\mathbf{T}_\tau^0(\mathbf{v})\|^2_{L^2(\Gamma)}}{\displaystyle\int_\Omega \boldsymbol{\sigma}(\mathbf{v}):\boldsymbol{\varepsilon}(\mathbf{v})d\mathbf{x}}. \tag{26}$$

For $\theta=-1$, this condition reduces to $\beta_n^0>0$ and $\beta_\tau^0>0$ showing the additional robustness of the Nitsche's method for this value of the parameter. This well-posedness analysis readily extends to the mean-Nitsche's method replacing $T_n^0(\mathbf{v})$ and $\mathbf{T}_\tau^0(\mathbf{v})$ by $\pi_{\mathcal{F}}^0T_n^0(\mathbf{v})$ and $\pi_{\mathcal{F}}^0\mathbf{T}_\tau^0(\mathbf{v})$ in the above definitions. An existence result for the Coulomb friction model is also derived in [23] using the Brouwer fixed point theorem based on the Tresca friction solution.

Optimal a priori error estimates in the natural norm have been established in [22] for frictionless contact (see also [20] for Tresca friction and [21] for an overview of the results). They are readily adapted to the poromechanical model with pressures source terms.

4 Numerical experiments for the Contact Mechanical model

The objective of this numerical section is to compare the accuracy, the convergence and the efficiency in terms of non-linear convergence of the mixed, stabilized mixed and Nitsche's methods described in the previous section. We restrict this study to triangular meshes using both $\mathbb{P}_1$ and $\mathbb{P}_2$ conforming Finite Element approximations $\mathbf{U}_h$ of the displacement field. Hence we consider the $\mathbb{P}_k$ Nitsche's discretization for $k\in\{1,2\}$ and the inf-sup stable $\mathbb{P}_2-\mathbb{P}_0$ mixed discretization using facewise $\mathbb{P}_0$ Lagrange multipliers. We also consider the $\mathbb{P}_k-\mathbb{P}_0$ stabilized mixed discretizations with degree $k\in\{1,2\}$ Finite Element approximation of the displacement field and facewise $\mathbb{P}_0$ Lagrange multipliers. They are formulated as Nitsche's methods by elimination of the Lagrange multipliers and termed $\mathbb{P}_k$ mean-Nitsche's discretizations in the following.

The non-linear systems are solved using a semi-smooth Newton algorithm. For the Nitsche's and mean-Nitsche's methods it just amounts to derive the functions $[x]_{\mathbb{R}^-}$, $x\in\mathbb{R}$, and $[\mathbf{x}]_\alpha$, $\mathbf{x}\in\mathbb{R}^{d-1}$ as piecewise linear functions in dimension $d=2$. The semi-smooth Newton algorithm of the $\mathbb{P}_2-\mathbb{P}_0$ mixed discretization is based on the equivalent semi-smooth formulation of the contact conditions (8). The non-linear stopping criteria is given for all discretizations by a relative norm of the residual set to 10^{-6} or a maximum Newton increment of 10^{-10} on the displacement field. At each Newton iteration, the linear system is solved using SuperLU 4.3 as a sparse direct solver. In the following tables reporting the numerical behavior of the numerical methods, $d.o.f$ denotes the number of geometrical degrees of freedom with 2 physical unknowns for each d.o.f., NZ is the number of geometrical non zero elements of the Jacobian system (each non zero element being a 2×2 matrix), $Newton$ is the number of semi-smooth Newton iterations and CPU denotes the total CPU time in seconds.

The computation of the errors and the plots along the fractures are based on continuous facewise $\mathbb{P}_k$ reconstructions of the displacement jumps and discontinuous facewise $\mathbb{P}_{k-1}$ reconstructions of the surface tractions for the degree k approximation of the displacement. A relaxation of the Newton increment can be used to obtain a more robust non-linear convergence. It is based on the prescription of a maximum Newton increment of the displacement field degree of freedom (d.o.f.) and component wise.

Note also that the Simpson rule is used for the numerical integration of the non-linear terms in the Nitsche's formulation on each fracture face. Higher order quadratures like Newton Cotes 7 and Gauss Legendre 5 have also been tested with a slight gain in accuracy but a significantly higher number of non-linear iterations.

4.1 Unbounded domain with single fracture under compression

This example was presented in [48, 28, 29]. It consists in a 2D unbounded domain containing a single fracture and subject to a compressive remote stress $\bar{\sigma} = 100\,\text{MPa}$ (cf. Figure 3). The fracture inclination with respect to the horizontal direction is $\psi = 20°$, its length is $2\ell = 2$ m, and the friction coefficient is $F = 1/\sqrt{3}$. The same values of Young's modulus and Poisson's ratio as in [28] are used here, i.e. $E = 25$ GPa and $\nu = 0.25$. The analytical solution in terms of normal surface traction and of the jump of the tangential displacement field, is given by

$$\overline{\lambda}_n = -T_n(\overline{\mathbf{u}}) = \bar{\sigma}\sin^2\psi, \quad |[\![\overline{\mathbf{u}}]\!]_\tau| = \frac{4(1-\nu)}{E}(\bar{\sigma}\sin\psi(\cos\psi - F\sin\psi))\sqrt{\ell^2 - (\ell^2-\tau^2)}, \quad (27)$$

where $0 \leqslant \tau \leqslant 2\ell$ is a curvilinear abscissa along the fracture. Note that since $\overline{\lambda}_n > 0$, we have $[\![\overline{\mathbf{u}}]\!]_n = 0$ on the fracture. Boundary conditions are imposed on $\mathbf{u}$ at specific nodes of the mesh, as shown in Figure 3, to respect the symmetry of the expected solution. For this simulation, we sample a $320 \times 320\,\text{m}^2$ square, and carry out uniform refinements at each step in such a way to compute the solution on meshes containing 100, 200, 400, and 800 faces on the fracture (corresponding, respectively, to 12 468, 49 872, 199 488, and 797 952 triangular elements). The initial mesh is refined in a neighborhood of the fracture; starting from this mesh, we perform global uniform refinements at each step, i.e. we do not refine further near the fracture.

The Nitsche's parameters are fixed to $\beta_0^n = 10^4$ GPa and $\beta_\tau^0 = 10^3$ GPa and $\theta = -1$ for all Nitsche's and mean-Nitsche's methods. The motivations behind these choices are postponed to paragraph 4.3.1.

Figure 4 shows the comparison between the analytical and numerical normal surface tractions T_n and jumps of the tangential displacement on the fracture $[\![\mathbf{u}]\!]_\tau$. These solutions are computed on the coarsest mesh with 100 fracture faces. As in [28], the normal surface traction T_n presents some oscillations in a neighborhood of the fracture tips. As already explained in [28], this is due to the sliding of faces close to the fracture tips (notice that all fracture faces are in a contact-slip state).

Figure 5 shows the convergence properties of the 5 numerical methods. Because of the oscillations of the approximation T_n close to the fracture tips, as in [28], we consider the central 90% of the fracture size to compute the norm of the error. Notice also that, since $[\![\overline{\mathbf{u}}]\!]_n = 0$, the relative error on the normal jump on the fracture is not defined.

For this test case, the accuracy of the discretizations depends mainly on the degree of approximation of the displacement field. In particular, except for the normal displacement jump, the $\mathbb{P}_2$ Nitsche's, mean-Nitsche's and mixed methods provide very closed solutions and convergence behavior. The same holds for the $\mathbb{P}_1$ Nitsche's and mean-Nitsche's methods.

A much better accuracy is obtained for $\mathbb{P}_2$ than for $\mathbb{P}_1$ discretizations of the displacement field. The order of convergence is of order 1 on the displacement jumps for all methods. This is related to the low regularity of $[\![\overline{\mathbf{u}}]\!]$ close to the tips (cf. the analytical expression (27)). The rate of convergence for the surface tractions is roughly equal to the degree of approximation (2 for $\mathbb{P}_2$ and 1 for $\mathbb{P}_1$), which is likely related to the fact that $T_n(\overline{\mathbf{u}})$ is constant. Sub-figure 5 (d) compares the errors for the Nitsche's $\mathbb{P}_1$ and $\mathbb{P}_2$ methods as a function of the number of non-zero elements in the Jacobian matrices. It shows that for a scalable linear solver, the best performance is obtained for the $\mathbb{P}_2$ approximation.

Note also that, for the rather high chosen Nistche parameters β_n^0 and β_τ^0, the solutions of the $\mathbb{P}_2$ mean-Nitsche's and mixed methods almost fully match with a higher value of the error on the normal displacement jump compared with other methods due to stronger oscillations at the tips. The lowest errors on the normal displacement jump are obtained for the $\mathbb{P}_k$ Nitsche's methods $k \in \{1, 2\}$. It was expected since they would provide, for such vanishing exact solution $T_n(\overline{\mathbf{u}})$ and assuming exact quadrature, an error on the normal displacement jump that will tend to 0 with Nitsche's parameter β_n^0 going to infinity.

In Table 1, we give an insight into the computational performance of the semi-smooth Newton algorithms for the 5 numerical methods.

	Nitsche $\mathbb{P}_2$	mean-Nitsche $\mathbb{P}_2$	mixed $\mathbb{P}_2 - \mathbb{P}_0$	Nitsche $\mathbb{P}_1$	mean-Nitsche $\mathbb{P}_1$
d.o.f.	400 k	400 k	400 k	100 k	100 k
NZ	4 622 k	4622 k	4603 k	707 k	707 k
Newton	2	2	2	4	2
CPU (s)	288	286	293	31	17

Table 1: Performance of the semi-smooth Newton algorithm for the 5 numerical methods for the example of Section 4.1. Triangular mesh with 199 488 cells and 400 fracture faces.

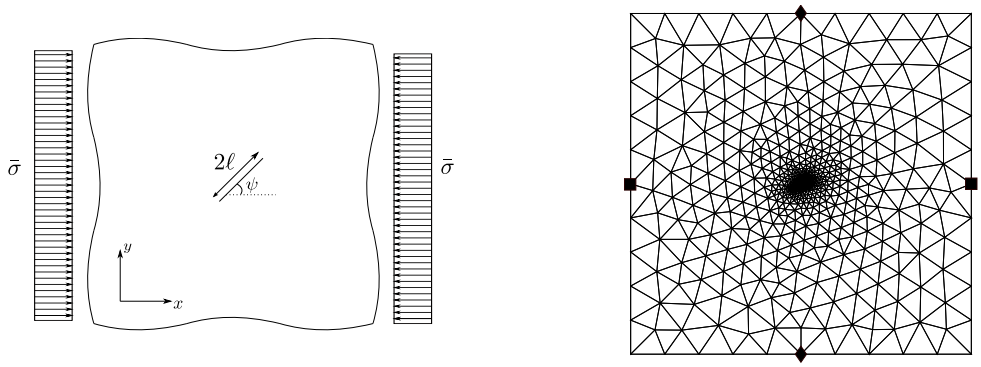

(a) (b)

Figure 3: Unbounded domain containing a single fracture under uniform compression (a) and mesh including nodes for boundary conditions (♦: $u_x = 0$, ■: $u_y = 0$), for the example of Section 4.1.

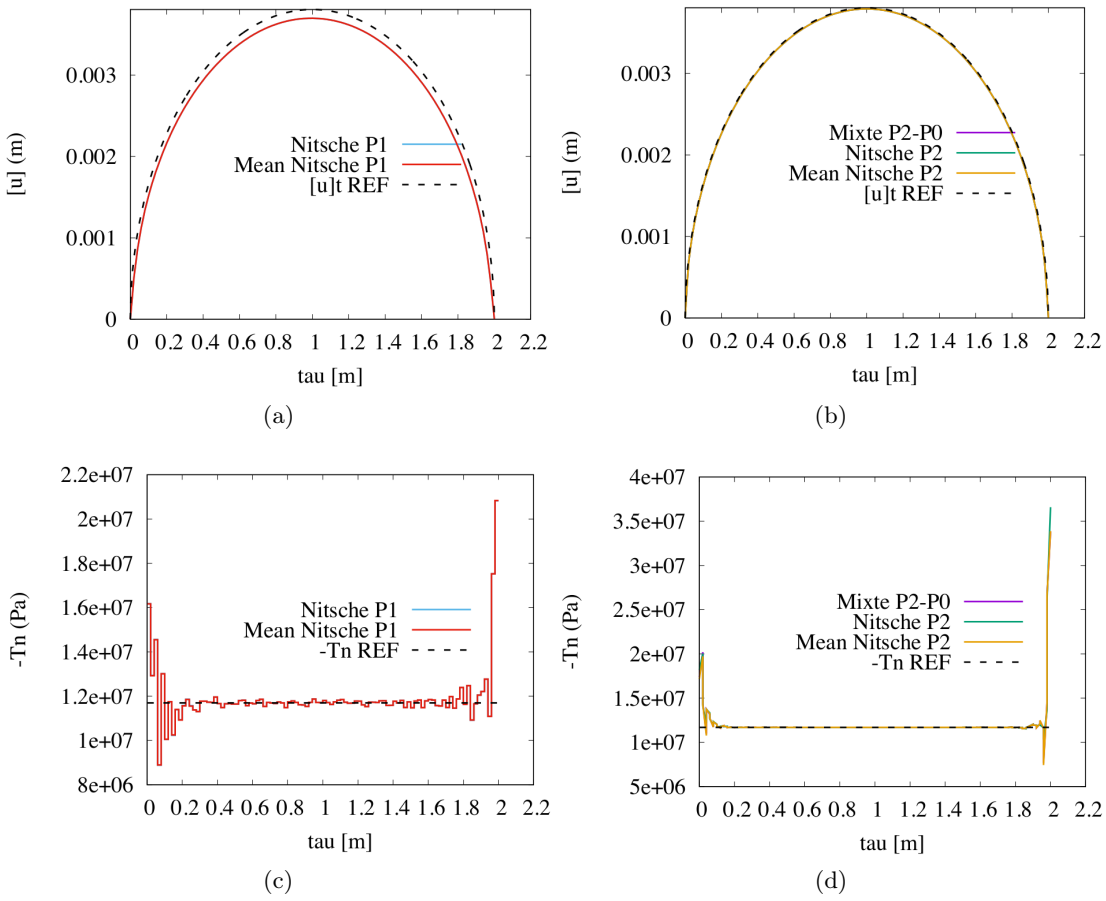

(a) (b)

(c) (d)

Figure 4: Comparison of the coarse mesh (with 100 fracture faces) numerical and analytical (labeled as REF) solutions in terms of $[\![\mathbf{u}]\!]_\tau$ (a) and (b) and T_n (c) and (d), for the example of Section 4.1.

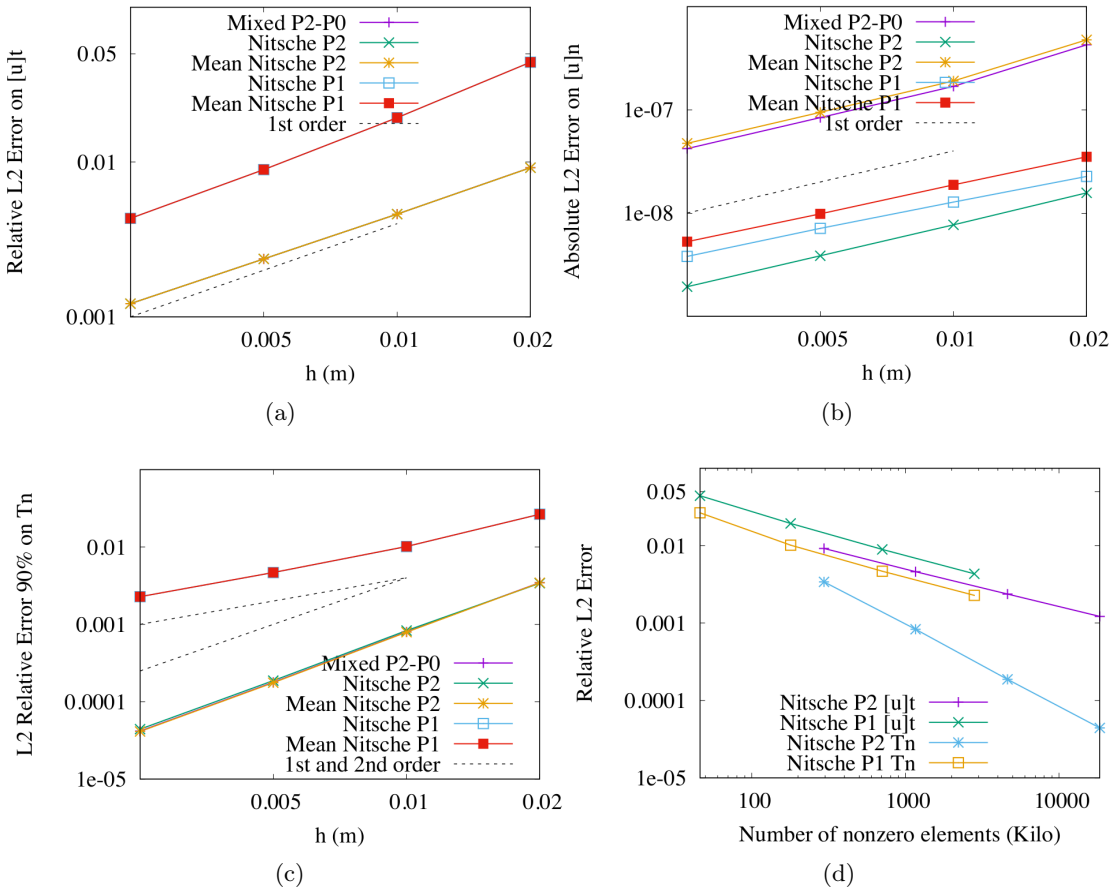

Figure 5: Relative and absolute L^2 errors between the numerical and analytical solutions in terms of $[\![\mathbf{u}]\!]_n$, $[\![\mathbf{u}]\!]_\tau$ and T_n, for the example of Section 4.1. The sub-figures (a),(b),(c) plot the errors as a function of h and the sub-figure (d) plots the errors as a function of the number of non-zero elements of the Jacobian matrices.

4.2 Cross shaped fracture network

This test case considers the DFM model exhibited in Figure 6 with a cross shaped fracture network immersed in the domain $\Omega = (0, 1\,\mathrm{m})^2$. Young's modulus and Poisson's ratio are homogeneous and fixed to $E = 4$ GPa and $\nu = 0.2$. The friction coefficient is fixed to $F = 0.5$. Regarding boundary conditions, the left and right boundaries are free, the bottom boundary is clamped and a Dirichlet boundary condition is imposed on the top boundary defined by $\mathbf{u}(\mathbf{x}) = [0.004\,\mathrm{m}, -0.0002\,\mathrm{m}]^\top$.

We compare in the following the accuracy, convergence and numerical performances of the 5 numerical methods. The $\mathbb{P}_k$ Nitsche's and mean-Nitsche's methods, $k \in \{1, 2\}$, use the parameters $\beta_n^0 = 1000$ GPa, $\beta_\tau^0 = 40$ GPa and $\theta = -1$. The motivations behind these choices is postponed to paragraph 4.3.1. The parameter of the semi-smooth Newton algorithm of the $\mathbb{P}_2 - \mathbb{P}_0$ mixed method is fixed to $\beta^{\mathrm{sm}} = 1$ GPa.

No analytical solution is available for this test case. We therefore investigate the convergence of

our discretizations by computing a reference solution on a fine mesh made of $896 \times 4^4 = 229\,376$ triangular elements and $2^8 = 256$ fracture faces using the $\mathbb{P}_2$ Nitsche's method with the Newton Cotes 7 points quadrature formula for the numerical integration of the non-linear terms. The meshes $m \in \{0, \cdots, 3\}$ used for the convergence plots have 896×4^m triangular cells and 2^{m+4} fracture faces.

As exhibited in Figure 6 (b) and (c), for the chosen boundary conditions, both fractures are in full contact mode, the horizontal fractures being in slip mode and the vertical fractures exhibiting a transition between stick mode at the center and slip mode around the tips. The comparison below focuses on the normal and tangential displacement jumps and surface tractions along the vertical fractures which are more challenging due to the stick slip transitions.

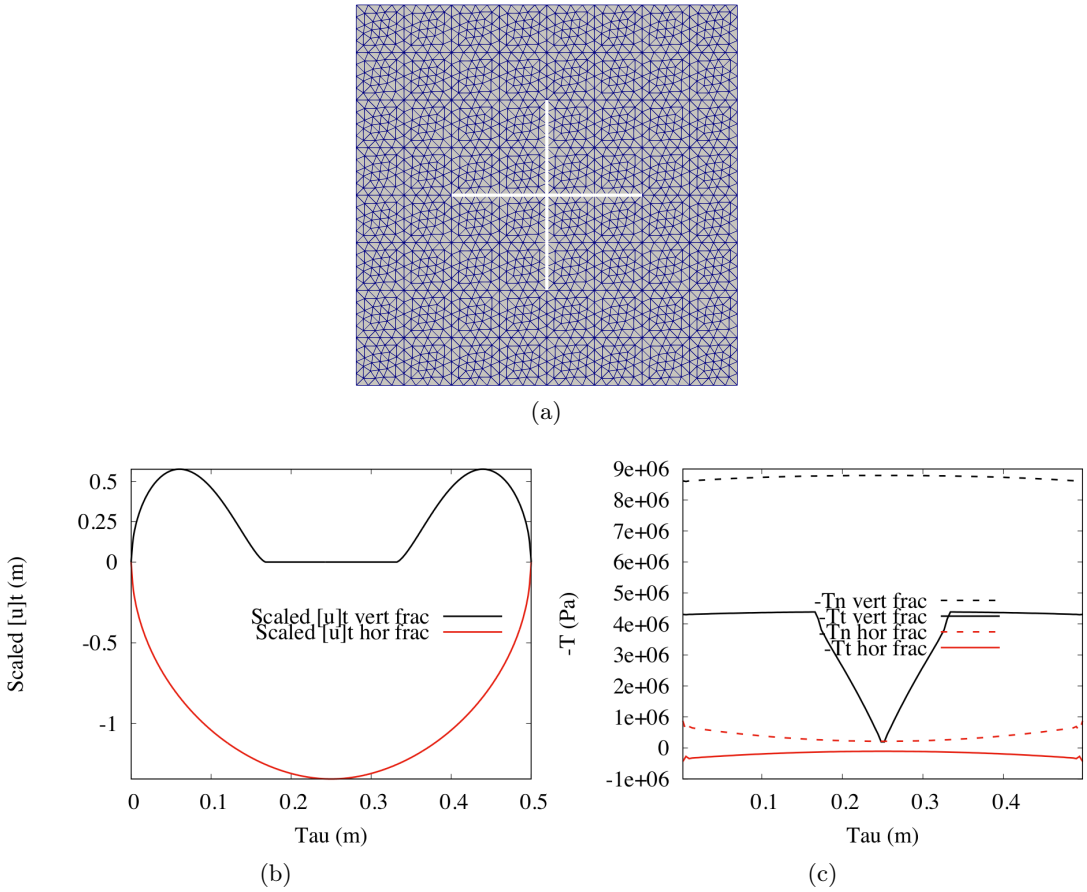

Figure 6: (a) square domain $(0, 1\,\mathrm{m})^2$ containing a cross shaped fracture network and its coarsest triangular mesh with 3584 cells and 32 fracture faces. (b) and (c) fine mesh reference solutions for the displacement tangential jump $[\![\mathbf{u}]\!]_\tau$ and normal and tangential surface tractions $-T_n$ and $-T_\tau$ along the vertical and horizontal fractures.

Figure 7 compares the coarse mesh $m = 0$ and reference solutions along the vertical fractures. It shows the higher accuracy provided by degree 2 compared with degree 1 approximations especially for the surface tractions. The $\mathbb{P}_k$ mean-Nitsche's and $\mathbb{P}_2 - \mathbb{P}_0$ mixed methods exhibit oscillations of the normal and tangential displacement jumps in the regions where these jumps vanish. These oscillations of amplitudes reducing with the mesh size are due to the fact that

the contact conditions are only imposed on the mean values of the displacement jumps and surface tractions over each fracture face. This is not the case of the $\mathbb{P}_k$ Nitsche's methods. Consequently the $\mathbb{P}_2$ Nitsche's discretization is clearly the most accurate of all the 5 numerical methods for this test case.

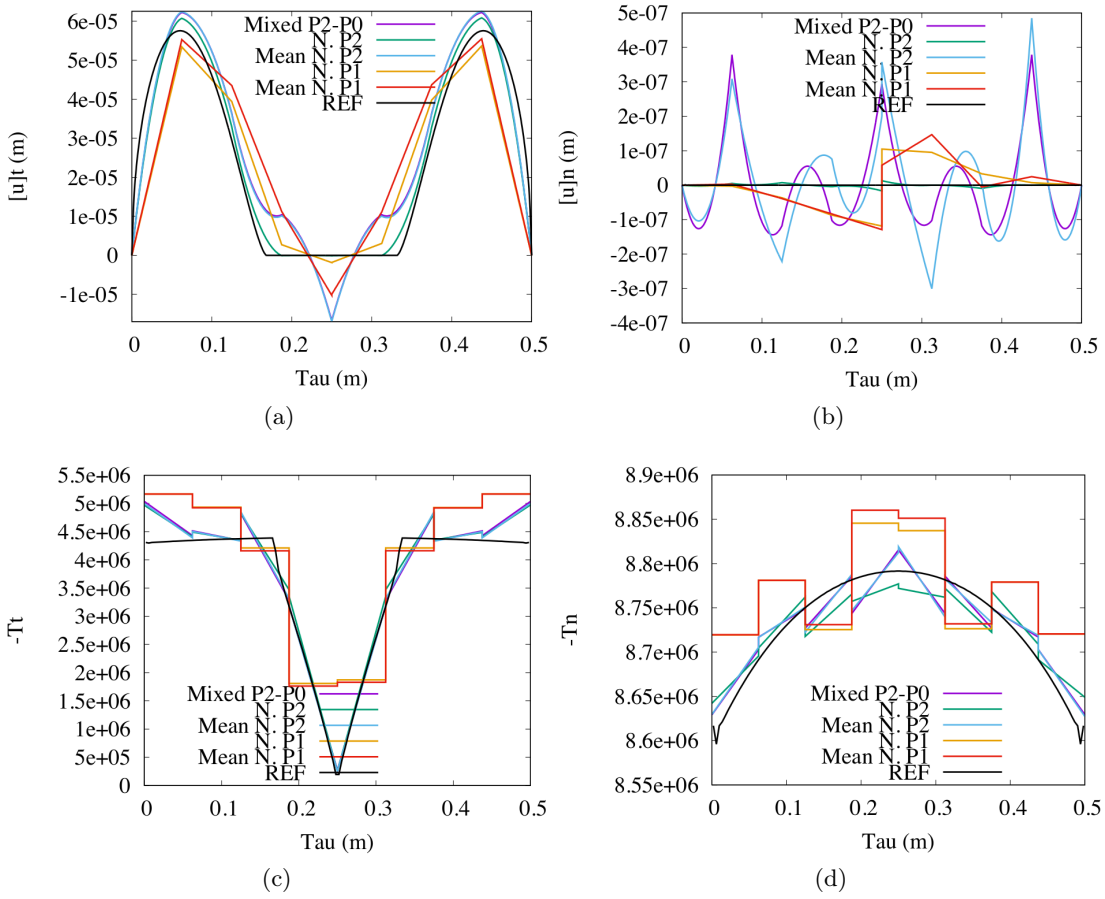

Figure 7: Comparison of the coarse mesh $m = 0$ and fine mesh reference (in black line and labeled as REF) solutions in terms of $[\![\mathbf{u}]\!]_\tau$ (a), $[\![\mathbf{u}]\!]_n$ (b), $-T_\tau$ (c) and $-T_n$ (d) along the vertical fractures, for the example of Section 4.2.

Figure 8 plots the convergence of the L_2 errors along the vertical fractures for the displacement jumps and surface tractions. It shows again the higher accuracy provided by the degree 2 approximations with higher convergence rates for the tangential displacement jumps and surface tractions. The mixed and mean methods behave roughly speaking in the same way than the full Nitsche's discretizations of same degree, except for the vanishing normal displacement jump due to the previously mentioned higher oscillations induced by the face averaging of the contact conditions.

Figure 9 plots the convergence of the errors as a function of the number of Jacobian non-zero elements for the $\mathbb{P}_k$ Nitsche's methods of degree $k \in \{1, 2\}$. It shows that the degree 2 approximation is more efficient especially for the surface traction.

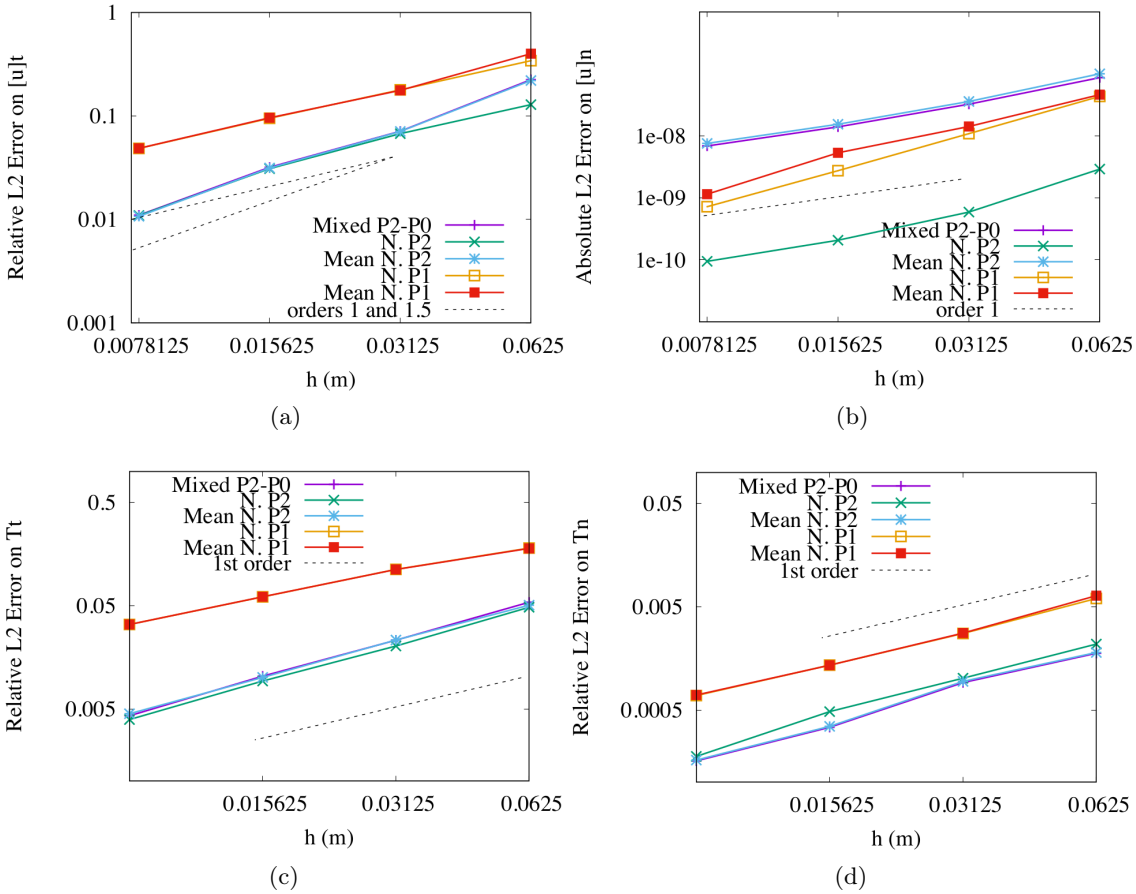

Figure 8: Relative and absolute L^2 errors between the mesh $i \in \{0, \cdots, 3\}$ and fine reference solutions in terms of $[\![\mathbf{u}]\!]_\tau$ (a), $[\![\mathbf{u}]\!]_n$ (b), T_τ (c) and T_n (d) along the vertical fractures for the example of Section 4.2.

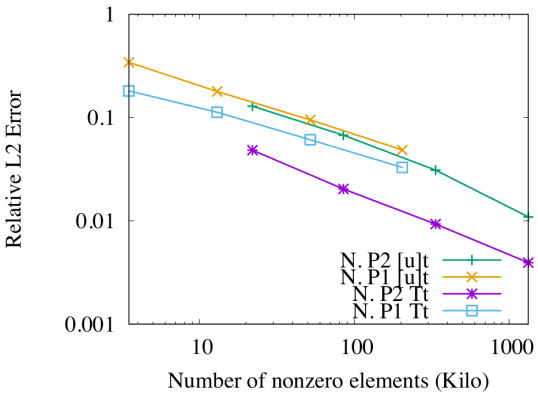

Figure 9: Relative L^2 error between the mesh $i \in \{0, \cdots, 3\}$ and fine reference solutions in terms of $[\![\mathbf{u}]\!]_\tau$ and T_τ along the vertical fractures as a function of the number of non-zero elements of the Jacobian matrices for the example of Section 4.2.

Table 2 exhibits the numerical performances of the 5 numerical methods on mesh $m = 3$. The semi-smooth Newton solvers behave roughly in the same way except the $\mathbb{P}_1$ Nitsche's method which requires an adaptive relaxation of the Newton step to obtain convergence. This issue can also be solved using the lower order trapezoidal rather than Simpson quadrature formula for the integration of the non-linear terms yielding almost the same accuracy and only 6 semi-smooth Newton iterations. A factor from 5 to 10 is observed in CPU time between degree 2 and 1 approximations. It is expected to be significantly reduced by using more scalable preconditioned iterative linear solvers which is out of the scope of this work.

	Nitsche $\mathbb{P}_2$	mean-Nitsche $\mathbb{P}_2$	mixed $\mathbb{P}_2 - \mathbb{P}_0$	Nitsche $\mathbb{P}_1$	mean-Nitsche $\mathbb{P}_1$
d.o.f.	115 k	115 k	116 k	29 k	29 k
NZ	1331 k	1331 k	1325 k	204 k	204 k
Newton	7	6	6	20	8
CPU (s)	140	120	115	22.5	12

Table 2: Performance of the semi-smooth Newton algorithm for the 5 numerical methods for the example of Section 4.2. Triangular mesh $m = 3$ with 896×4^3 cells and 2^7 fracture faces.

4.3 Rectangular domain with 6 fractures

As a more complex example to illustrate the behavior of our approach, we consider the test case presented in [6, Section 4.1], where a $2 \times 1\,\mathrm{m}$ domain including a network $\Gamma = \bigcup_{i=1}^{6} \Gamma_i$ of six fractures is considered, cf. Figure 10. Fracture 1 is made up of two sub-fractures forming a corner, whereas one of the tips of fracture 5 lies on the boundary of the domain.

We use the same values of Young's modulus and Poisson's ratio, $E = 4$ GPa and $\nu = 0.2$, and the same set of boundary conditions as in [6], that is, the two vertical sides of the domain are free, and we impose $\mathbf{u} = \mathbf{0}$ on the bottom side and $\mathbf{u} = [0.005, -0.002]^\top$ m on the top side. The friction coefficient is $F_i(\mathbf{x}) = 0.5\left(1 + 10\exp(-D_i(\mathbf{x})^2/0.005\,\mathrm{m}^2)\right)$, with $i \in \{1, \ldots, 6\}$ the fracture index, $\mathbf{x} \in \Gamma_i$ a generic point on fracture i and $D_i(\mathbf{x})$ the minimum distance from $\mathbf{x}$ to the tips of fracture i (the bend in fracture 1 is not considered as a tip).

To investigate the convergence of the 5 numerical methods, we consider a family of 5 uniformly refined meshes $m \in \{0, \cdots, 4\}$ with 2855×4^m triangular cells and 88×2^m fracture faces. The finest mesh $m = 4$ is used for the reference solution computed by the $\mathbb{P}_2$ Nitsche's method with the Newton Cotes 7 points quadrature for the integration of the non-linear terms.

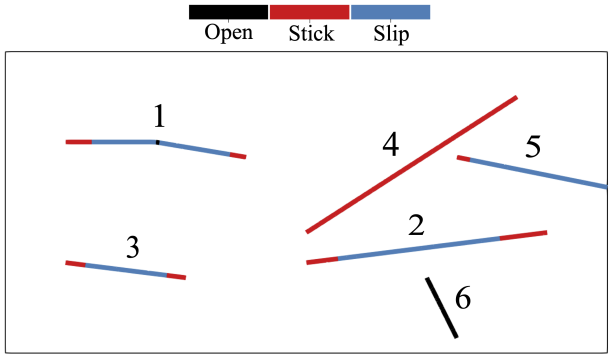

Figure 10: Two-dimensional, $2 \times 1\,\mathrm{m}$ domain containing six fractures. Fracture 1 comprises two sub-fractures making a corner and fracture 5 has a tip on the boundary. The contact state of each fracture obtained by the simulation on the fine mesh is also shown.

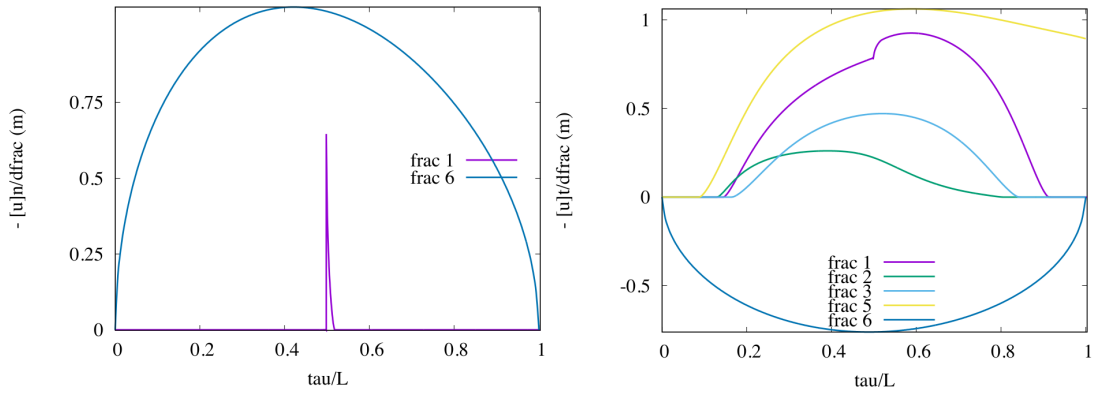

Figure 11: Scaled normal (a) and tangential (b) displacement jumps for the fine mesh reference solution (the normal jumps of the fractures 2,3,4,5 in full contact mode and the tangential jump of fracture 4 in full stick mode are not plotted). Example of Section 4.3.

4.3.1 Choice of the Nitsche's parameters β_n^0, β_τ^0 and θ

This choice is guided by both the robustness of the non-linear convergence and the accuracy. As a rule of thumb, the larger the Nitsche's penalization parameters, the better from the point of view of accuracy. The condition (25) provides lower bounds to guarantee the stability of the Tresca friction model. This condition is restrictive for $\theta = 0, 1$ but not for $\theta = -1$. For this test case, we obtain roughly for all meshes the following values of the eigenvalues γ_n and γ_τ defined by (26): $\gamma_n = 35$ GPa, $\gamma_\tau = 11$ GPa for both the $\mathbb{P}_2$ Nitsche's and mean-Nitsche's methods, and $\gamma_n = 11$ GPa, $\gamma_\tau = 3$ GPa for both the $\mathbb{P}_1$ Nitsche's and mean-Nitsche's methods. For Coulomb friction, the existence result from [23] is based on a fixed point Brouwer theorem related to the Tresca friction solution and assumes additional large enough conditions on the Nitsche's parameters to obtain the continuity of the fixed point function.

Figure 12 exhibits the number of semi-smooth Newton iterations as a function of $(\beta_n^0, \beta_\tau^0)$ for the $\mathbb{P}_2$ Nitsche's method with $\theta = 1, 0, -1$. It also plots the number of semi-smooth Newton iterations for the $\mathbb{P}_2 - \mathbb{P}_0$ mixed method as a function of the semi-smooth Newton parameters $(\beta_n^{\rm sm}, \beta_\tau^{\rm sm})$. A relaxation with maximum variation of 10^{-4} on the displacement field is used for the Nitsche's methods. The simulations are performed on the coarsest mesh $m = 0$.

The mixed method is remarkably robust w.r.t. the semi-smooth Newton parameters. The semi-smooth Newton fails to converge for the Nitsche's method when the parameter β_τ^0 is larger than say 10^{12} whatever β_n^0 and $\theta = 1, 0, -1$. This limitation is not observed for large values of the parameter β_n^0 and has not been observed for frictionless contact. This observation motivates the use of two distinct values of these parameters in the following.

The combination of the Tresca stability criteria and the observed non-linear convergence shows that $\theta = -1$ is the most robust choice w.r.t. to the range of admissible Nitsche's parameters. This motivates the choice of $\theta = -1$ with $\beta_n^0 = 1000$ GPa and $\beta_\tau^0 = 100$ GPa in the following numerical experiments.

Similar conclusions are obtained for the $\mathbb{P}_1$ Nitsche's and $\mathbb{P}_1$ mean-Nitsche's methods. The case of the $\mathbb{P}_2$ mean-Nitsche's method differs in the sense that it converges to the $\mathbb{P}_2 - \mathbb{P}_0$ mixed method when $\min(\beta_n^0, \beta_\tau^0)$ tends to $+\infty$. As a result, it can be checked to be robust for large values of both parameters.

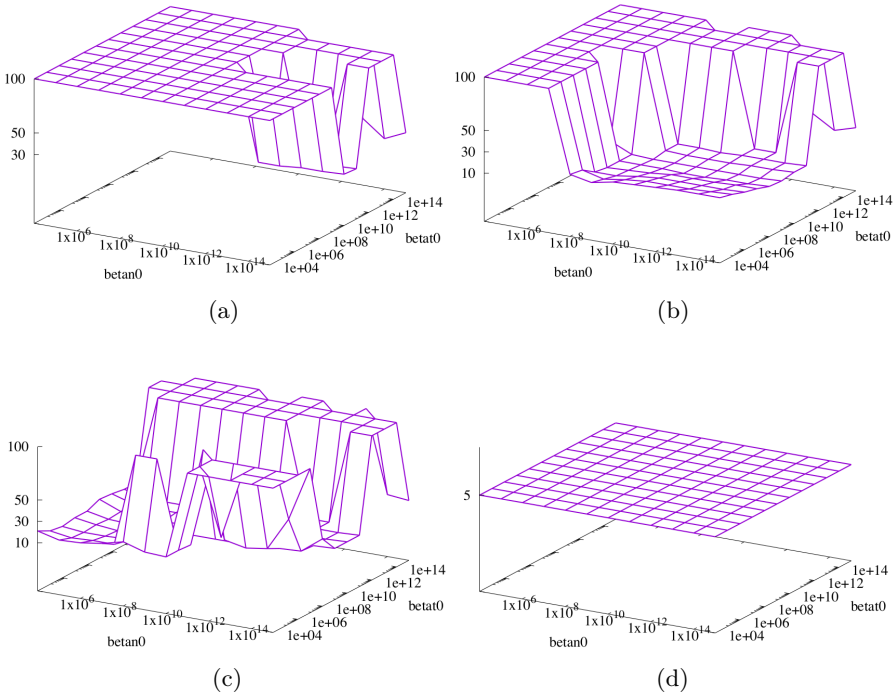

Figure 12: (a),(b),(c) for respectively $\theta = 1, 0, -1$ and the $\mathbb{P}_2$ Nitsche's method on the coarsest mesh, number of semi-smooth Newton iterations as a function of $(\beta_n^0, \beta_\tau^0)$. (d) for the $\mathbb{P}_2 - \mathbb{P}_0$ mixed method on the coarsest mesh $m = 0$, number of semi-smooth Newton iterations as a function of $(\beta_n^{\rm sm}, \beta_\tau^{\rm sm})$. Example of Section 4.3.

4.3.2 Convergence of the $\mathbb{P}_2$ mean-Nitsche's method to the $\mathbb{P}_2-\mathbb{P}_0$ mixed method

Figure 13 checks numerically the convergence of the $\mathbb{P}_2$ mean-Nitsche's solution to the mixed solution. To fix ideas we restrict ourselves to the case $\beta_n^0 = 2.5\beta_\tau^0 = \beta^0$. The mesh $m = 1$ is used for these computations. As expected, we observe for sufficiently large values of β^0 a convergence of order 1 of the mean-Nitsche's solution to the solution of the mixed method on the same mesh.

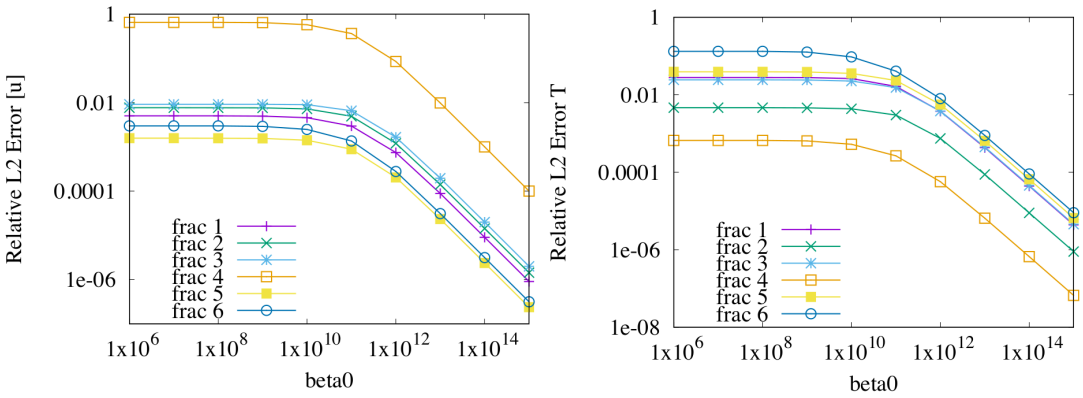

Figure 13: Convergence of the relative L^2 error of the displacement jump (a) and the surface traction (b) along each fracture between the mesh 1 solutions of the mixed and $\mathbb{P}_2$ mean-Nitsche's methods as a function of the parameter $\beta^0 = \beta_n^0 = 2.5\beta_\tau^0$. Example of Section 4.3.

4.3.3 Comparison of the 5 numerical methods

In this paragraph, we compare the numerical convergence on the four meshes $m \in \{0, \cdots, 3\}$ of the 5 numerical methods using the fine mesh reference solution. In accordance with the previous paragraphs, the Nitsche's parameters are fixed to $\beta_n^0 = 1000$ GPa, $\beta_\tau^0 = 100$ GPa and $\theta = -1$.

Figures 14 and 15 plot the convergence of the relative L^2 errors on respectively the displacement jumps and surface tractions along each fracture, excluding fracture 4 for the jump and fracture 6 for the surface traction the solution of which vanish at convergence. The conclusions are similar as in the previous test cases, showing a more accurate approximation of the $\mathbb{P}_2$ compared with the $\mathbb{P}_1$ approximations of the displacement field. Among the methods of same degree of approximation for the displacement field, the Nitsche's methods are more accurate in singularity regions than mean-Nitsche's/mixed methods based on face averaging (particularly for fracture 1 in this test case) while they are very closed in smooth regions. This can be checked in Figure 16 plotting the coarse mesh $m = 0$ displacement jumps along fracture 1,3 and 6. It is shown that the mean-Nitsche's/mixed methods are oscillating in singularity zones (transition zones for fractures 1 and 3) due to the face averaging. The higher accuracy of degree 2 methods is also clearly observed.

The performance of the non-linear solvers are exhibited in Table 3 on the mesh $m = 3$. A relaxation of the Newton step is used for the Nitsche's and mean-Nitsche's methods while it

happens to be useless for the mixed method (here using $\beta_n^{\rm sm} = \beta_\tau^{\rm sm} = 1$ GPa) which is the most efficient and robust in terms of non-linear convergence. Note that the non-linear convergence of the Nitsche's and mean-Nitsche's methods improve for smaller values of the parameters β_n^0 and β_τ^0. For $\beta_n^0 = 100$ GPa and $\beta_\tau^0 = 20$ GPa, the number of Newton iterations reduces to 10,9,12,10 for respectively the $\mathbb{P}_2$ Nitsche's, mean-Nitsche's and the $\mathbb{P}_1$ Nitsche's and mean-Nitsche's methods, with similar accuracy except some rather small additional oscillations in singularity zones for both Nitsche's methods. Much lower values $\beta_n^0 = 0.1$ GPa and $\beta_\tau^0 = 0.01$ GPa have also been tested with additional robustness of the non-linear solver but at the expense of a loss of accuracy except for the $\mathbb{P}_2$ mean-Nitsche's method which is the most robust both in terms of accuracy and non-linear convergence w.r.t. to the Nitsche's parameters.

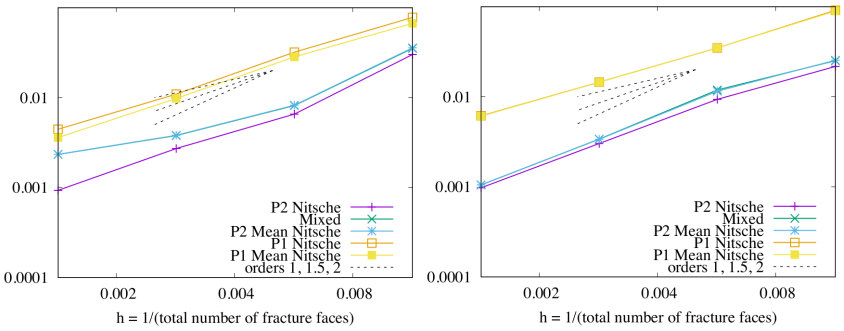

(a) fracture 1 (b) fracture 2

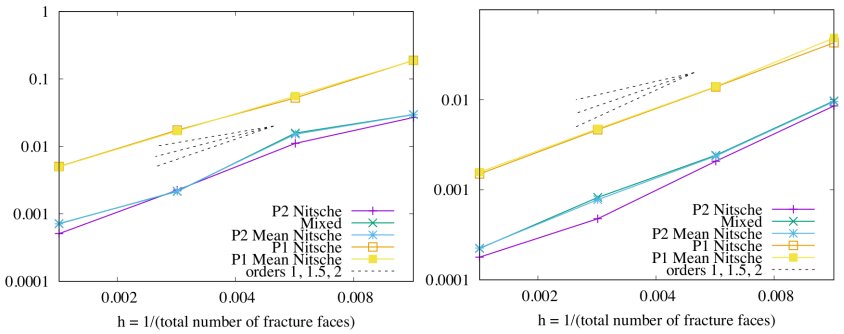

(c) fracture 3 (d) fracture 5

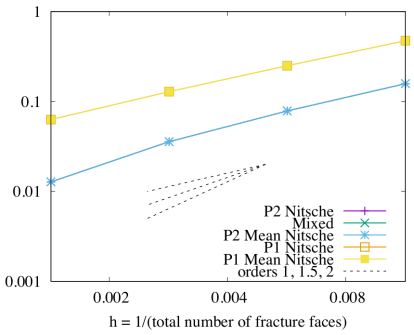

(e) fracture 6

Figure 14: Convergence of the relative L^2 error of the displacement jump along fractures 1,2,3,5,6 for the 5 numerical methods. Example of Section 4.3.

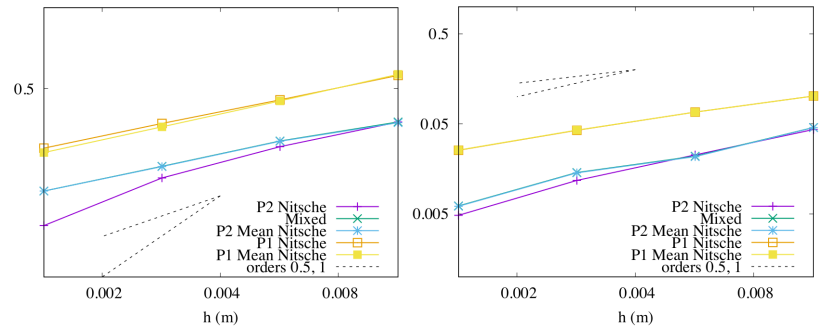

(a) fracture 1

(b) fracture 2

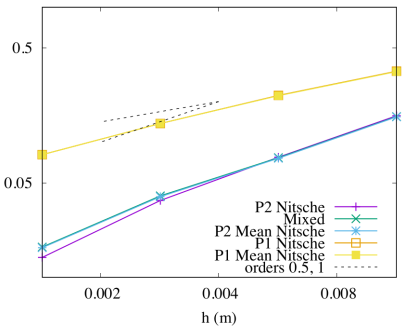

(c) fracture 3

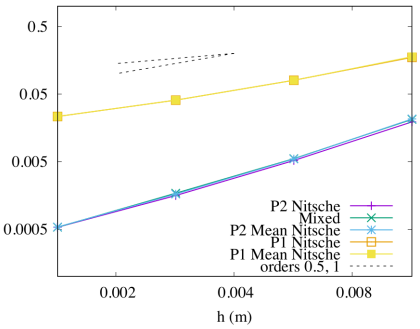

(d) fracture 4

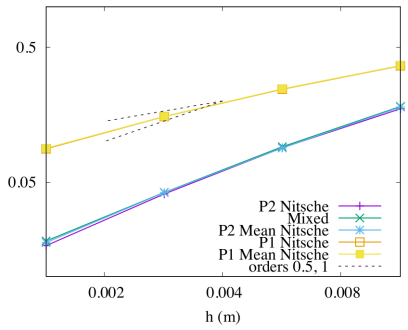

(e) fracture 5

Figure 15: Convergence of the relative L^2 error of the surface traction along fractures 1,2,3,4,5 for the 5 numerical methods. Example of Section 4.3.

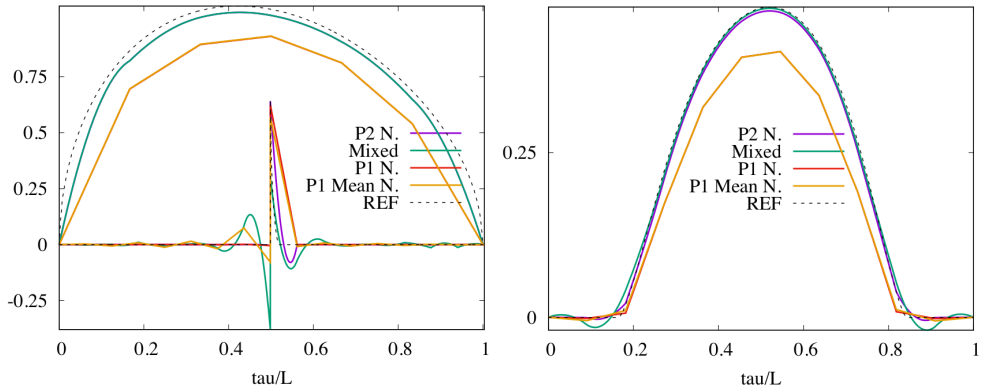

(a) (b)

Figure 16: Scaled normal (a) and tangential (b) displacement jumps for respectively fractures 1 and 6, and for fracture 3, on the coarse mesh $m = 0$ for the different discretizations (the $\mathbb{P}_2$ mean-Nitsche's basically matches with the mixed solution, hence it is not plotted). Example of Section 4.3.

	$\mathbb{P}_2$ Nitsche	$\mathbb{P}_2$ mean-Nitsche	mixed $\mathbb{P}_2 - \mathbb{P}_0$	$\mathbb{P}_1$ Nitsche	$\mathbb{P}_1$ mean-Nitsche
d.o.f.	368 k	368 k	369 k	93 k	93 k
NZ	4261 k	4261 k	4230 k	654 k	654 k
Newton	13	12	10	14	20
CPU (s)	1390	1385	1150	85	122

Table 3: Performance of the semi-smooth Newton algorithm for the 5 numerical methods for the example of Section 4.3. Triangular mesh $m = 3$ with 2855×4^3 cells and 88×2^3 fracture faces.

5 Coupled poromechanical simulation

The objective of this section is to compare the efficiency of the Nitsche's and mixed formulations to simulate the fully coupled poromechanical model. The flow component (1a) is discretized in space by a mixed-dimensional Hybrid Finite Volume (HFV) scheme [1, 17]. The $\mathbb{P}_2$ approximation of the displacement field is prefered to guarantee the inf-sup stability of the pressure displacement coupling in order to avoid the development of pressure spurious modes that can occur for incompressible problems approaching the undrained conditions. The $\mathbb{P}_1$ approximation would require an additional stabilization as described e.g. in [15]. At each time step, the coupled non-linear system is solved using a fixed-point method on the function

$$\mathbf{g}_p : p \underset{\substack{\text{Contact Mechanics}\\ \text{Solve}}}{\rightarrow} \mathbf{u} \underset{\substack{\text{Darcy}\\ \text{Solve}}}{\rightarrow} \widetilde{p},$$

with $p = (p_m, p_f)$, accelerated by a Newton–Krylov algorithm [8] in order to obtain at convergence the fully coupled poromechanical solution. At each evaluation of the fixed point

function $\mathbf{g}_p$, the Darcy linear problem at given fracture aperture and porosity is solved using a GMRes iterative solver preconditioned by AMG while the contact mechanical model at given pressure p is solved using a semi-smooth Newton method as in the previous section.

As in in [6, Section 4.3], this test case basically adds the fluid flow to the mechanical test case of Subsection 4.3. Regarding the mechanical model, compared with Subsection 4.3, the only changes are related to the friction coefficient fixed here to $F = 0.5$ and to the following time dependent Dirichlet boundary conditions

$$\mathbf{u}(t, \mathbf{x}) = \begin{cases} [0.005\,\mathrm{m}, -0.002\,\mathrm{m}]^\top \, 4t/T & \text{if } t \leqslant T/4, \\ [0.005\,\mathrm{m}, -0.002\,\mathrm{m}]^\top & \text{otherwise,} \end{cases} \qquad \mathbf{x} \text{ on the top boundary.}$$

To fully exploit the capabilities of the HFV flow discretization, we consider the following anisotropic permeability tensor in the matrix:

$$\mathbb{K}_m = K_m \, \mathbf{e}_x \otimes \mathbf{e}_x + \frac{K_m}{2} \, \mathbf{e}_y \otimes \mathbf{e}_y,$$

$\mathbf{e}_x$ and $\mathbf{e}_y$ being the unit vectors associated with the x- and y-axes, respectively.

The permeability coefficient is set to $K_m = 10^{-15}$ m^2, the Biot coefficient to $b = 0.5$, the Biot modulus to $M = 10$ GPa, the dynamic viscosity to $\eta = 10^{-3}$ Pa·s. The initial matrix porosity is set to $\phi_m^0 = 0.4$ and the fracture aperture corresponding to both contact state and zero displacement field is given by

$$d_0(\mathbf{x}) = \delta_0 \frac{\sqrt{\arctan(aD_i(\mathbf{x}))}}{\sqrt{\arctan(a\ell_i)}}, \quad \mathbf{x} \in \Gamma_i, \quad i \in \{1, \ldots, 6\},$$

where $D_i(\mathbf{x})$ is the distance from $\mathbf{x}$ to the tips of fracture i, $\delta_0 = 10^{-4}$ m, $a = 25$ m^{-1} and ℓ_i is a fracture-dependent characteristic length: it is equal to $L_i/2$ (L_i being the length of fracture i) if fracture i is immersed, to L_i if one of its ends lies on the boundary, and to the distance of a corner from tips, if it includes a corner. Note that the above expression behaves asymptotically as $\sqrt{D_i(\mathbf{x})}$ when $\mathbf{x}$ is close to fracture tips, which is in agreement with [31, Remark 3.1].

The normal transmissibility of fractures is set to $\Lambda_f = \frac{d_f}{6\eta}$. The initial pressure in the matrix and fracture network is $p_m^0 = p_f^0 = 10^5$ Pa. Notice that the initial fracture aperture differs from d_0, since it is computed by solving the mechanics given the initial pressures p_m^0 and p_f^0. The final time is set to $T = 2000$ s and the time integration uses an Euler implicit scheme with a uniform time stepping and 20 time steps. Concerning boundary conditions, for the flow, all sides are assumed impervious, except the left one, on which a pressure equal to the initial value 10^5 Pa is prescribed.

Figure 17 exhibits the contact state along the fractures at times $t = T/4$ for which the pressures reach their maximum values and at final time $t = T$ for which the pressures are almost back to their initial value as shown in Figure 18 for the matrix pressure. Given the Biot coefficient $b = 0.5$, this pressure decrease explains the switch from slip to stick state along the fractures at times larger than $T/4$. Note that the fracture pressure basically matches with the traces of the matrix pressure due to the high conductivity of the fractures.

Figure 19 plots the mean aperture as a function of time for the different meshes and the mixed and Nitsche's formulations. It shows that the Nitsche's method has a better convergence in space to the reference solution. It has been checked that the solution obtained with the mean-Nitsche's formulation is almost the same than the one of the mixed solution as expected for the inf-sup stable $\mathbb{P}_2 - \mathbb{P}_0$ approximation. Other mean quantities like the mean matrix and fracture pressures and the mean porosity as functions of time do not exhibit significant differences between both formulations. At the fracture scale, we can still observe the higher accuracy of the Nitsche's method in singularity regions.

Finally, Figure 20 plots the total number of semi-smooth Newton iterations for the contact mechanical model as a function of time. It shows that both the Nitsche's and mean-Nitsche's methods perform rather well compared to the mixed method which is the most efficient in terms of non-linear convergence. Note that the total number of fixed point function $\mathbf{g}_p$ evaluations is the same for all methods and both meshes and is equal to 190 for 20 time steps with a tight stopping criteria of 10^{-5} on the relative residual.

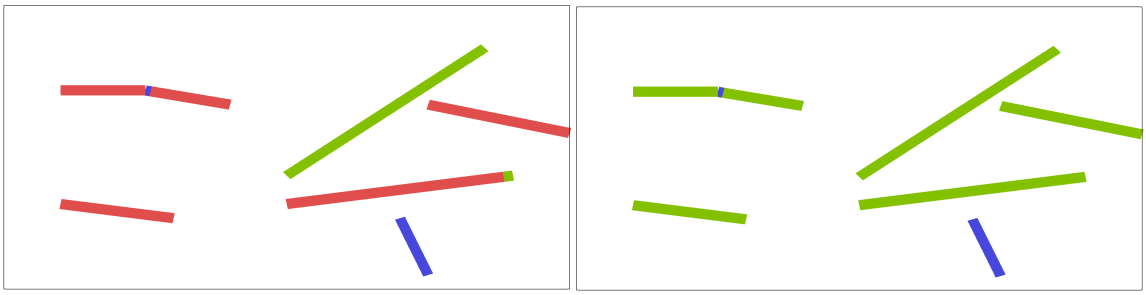

(a) (b)

Figure 17: Contact state along the fractures (blue: open, green: stick, red: slip) for the reference solution computed on the mesh $m = 3$ at times $t = T/4$ (a) and $t = T$ (b) . Example of Section 5.

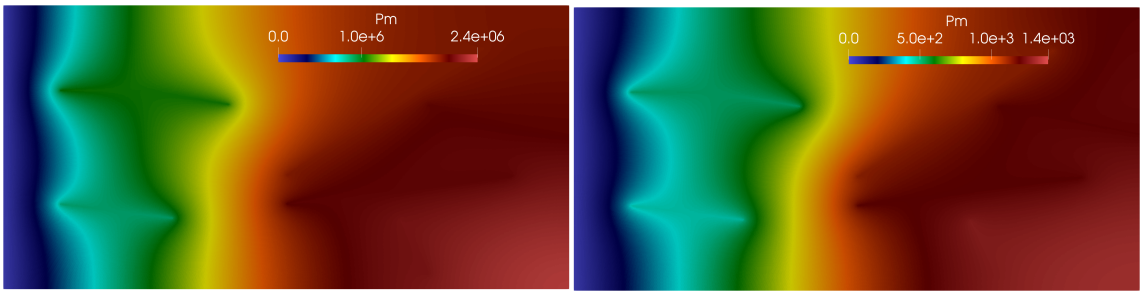

(a) (b)

Figure 18: Matrix over pressures (compared with the initial pressure) in Pa for the reference solution computed on the mesh $m = 3$ at times $t = T/4$ (a) and $t = T$ (b) . Example of Section 5.

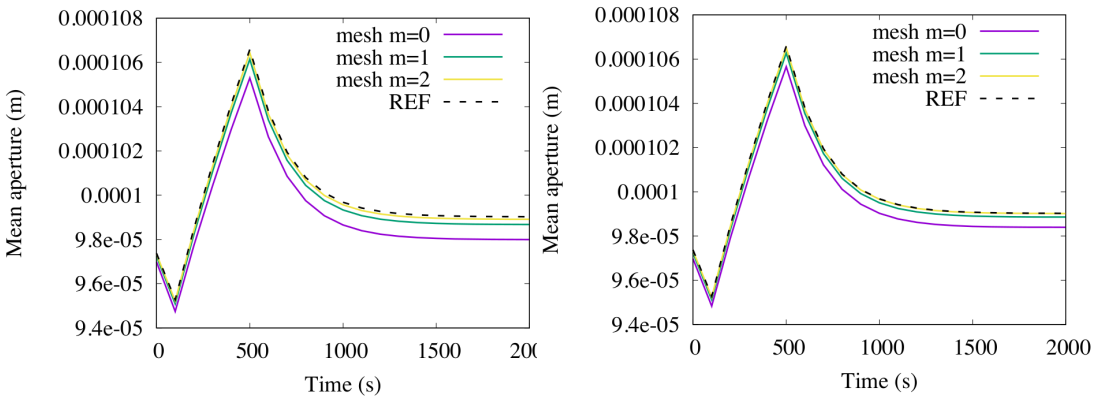

Figure 19: Mean aperture as a function of time for the mixed (a) and Nitsche's (b) formulations. The reference solution is computed using the mesh $m = 3$. Example of Section 5.

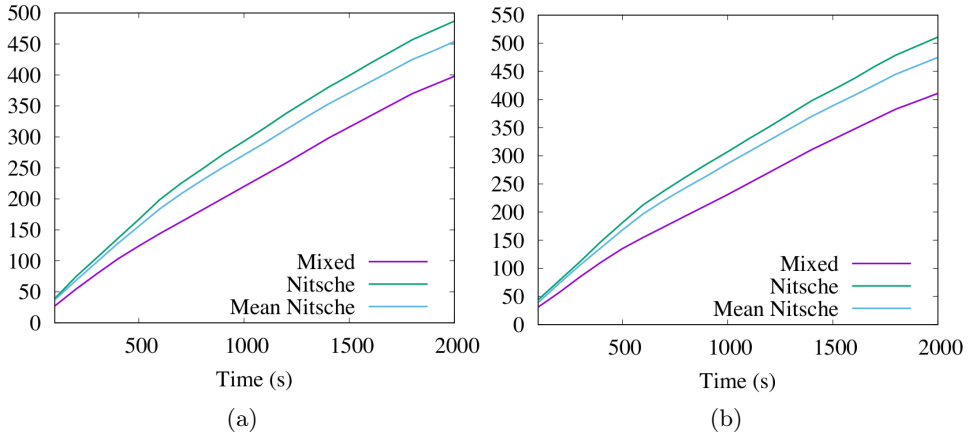

Figure 20: Total number of semi-smooth Newton iterations for the contact mechanical model as a function of time for the mixed, Nitsche's and mean-Nitsche's formulations using the meshes $m = 0$ (a) and $m = 1$ (b). Example of Section 5.

6 Conclusion

We investigated in this work mixed and Nitsche's formulations of the Coulomb frictional contact mechanics in mixed-dimensional poro-elastic models. We focused on mixed formulations based on facewise constant approximations of the Lagrange multipliers. This allows to deal efficiently with fracture intersections, corners and tips but on the other hand requires an inf-sup compatibility conditions between the displacement and the Lagrange multiplier discrete spaces. This restriction can be circumvented using a stabilized mixed formulation. Exploiting their facewise constant approximation, the Lagrange multipliers can be eliminated leading to a new so-called mean Nistche method based on face average tractions and displacement

jumps. This mean-Nitsche's method has two interesting features. It eliminates the Lagrange multiplier and do not require the inf-sup condition. It is also shown to converge to the mixed solution for large values of the Nitsche's parameters if we assume the inf-sup condition to hold. Several numerical experiments were performed in order to investigate and compare the three mixed, mean-Nitsche's, and Nitsche's formulations, both in terms of accuracy and of robustness of the non-linear solvers. We can draw the following conclusions from our numerical experiments.

- Nitsche's methods are more accurate than the mixed or mean-Nitsche's discretizations investigated in this work. It is due to additional oscillations in singularity zones (corners, intersections, transition zones) as a result of contact conditions based on face average quantities for the mixed and mean-Nitsche's methods.
- Regarding the Nitsche's parameter θ, the choice $\theta = -1$ clearly outperforms the other choices $\theta = 0, 1$ in terms of sensitivity of the non-linear convergence and accuracy to the Nitsche's parameters β_n^0 and β_τ^0.
- The parameters β_n^0 and β_τ^0 show a different behabior in terms of non-linear convergence which justifies the use of two a priori distinct parameters. The non-linear convergence is clearly much more sensitive to the parameter β_τ^0 (in particular for large values) than what is observed for β_n^0.
- The $\mathbb{P}_2$ approximations of the displacement field outperforms the $\mathbb{P}_1$ approximations in terms of accuracy for a given mesh. The final trade-off between cost and accuracy will depends on the scalability of the linear solver.
- As predicted by the analysis, the $\mathbb{P}_2 - \mathbb{P}_0$ mean-Nitsche's method allows to eliminate the Lagrange multipliers while providing almost the same results as the mixed method in terms of accuracy.
- The mixed method is the most robust in terms of non-linear convergence and sensitivity of the non-linear convergence to the semi-smooth Newton parameters.

In terms of perspectives, we intend to extend the discretization of mixed-dimensional poro-elastic models to polytopal meshes including non-matching meshes at matrix fracture interfaces. We would also like to investigate the well-posedness of the discrete coupled mixed-dimensional poro-elastic model. An existence result has been proved in [12] in the case of the mixed formulation based on a discrete energy estimate for the coupled model. This type of result is however still open in the case of the Nitsche's formulation of the contact mechanical model.

Acknowledgements: the authors would like to thank BRGM and Andra for partially supporting this work and authorizing its publication. Franz Chouly's work is partially supported by the I-Site BFC project NAANoD and the EIPHI Graduate School (contract ANR-17-EURE-0002). Franz Chouly is grateful of the Center for Mathematical Modeling grant FB20005.

References

[1] J. Aghili, K. Brenner, J. Hennicker, R. Masson, and L. Trenty. Hybrid finite volume discretization of two-phase discrete fracture matrix models with nonlinear interface solver. In *Conference Proceedings, ECMOR XVI*, volume 2018, pages 1–13. European Association of Geoscientists & Engineers, 2018.

[2] C. Alboin, J. Jaffre, J. Roberts, and C. Serres. Modeling fractures as interfaces for flow and transport in porous media. *Fluid flow and transport in porous media*, 295:13–24, 2002.

[3] P. Angot, F. Boyer, and F. Hubert. Asymptotic and numerical modelling of flows in fractured porous media. *ESAIM: Mathematical Modelling and Numerical Analysis*, 43(2):239–275, mar 2009.

[4] H. J.C. Barbosa and T. J.R. Hughes. The finite element method with lagrange multipliers on the boundary: circumventing the babuska-brezzi condition. *Computer Methods in Applied Mechanics and Engineering*, 85(1):109–128, 1991.

[5] F. Ben Belgacem and Y. Renard. Hybrid finite element methods for the Signorini problem. *Mathematics of Computation*, 72(243):1117–1145, 2003.

[6] R. L. Berge, I. Berre, E. Keilegavlen, J. M. Nordbotten, and B. Wohlmuth. Finite volume discretization for poroelastic media with fractures modeled by contact mechanics. *International Journal for Numerical Methods in Engineering*, 121:644–663, 2019.

[7] I. Berre, W. Boon, B. Flemisch, A. Fumagalli, D. Gläser, E. Keilegavlen, A. Scotti, I. Stefansson, A. Tatomir, K. Brenner, S. Burbulla, P. Devloo, O. Duran, M. Favino, J. Hennicker, I.-H. Lee, K. Lipnikov, R. Masson, K. Mosthaf, M.G.C. Nestola, C.-.F. Ni, K. Nikitin, P. Schädle, D. Svyatskiy, R. Yanbarisov, and P. Zulian. Verification benchmarks for single-phase flow in three-dimensional fractured porous media. *Advances in Water Resources*, 147:103759, 2021.

[8] F. Bonaldi, K. Brenner, J. Droniou, and R. Masson. Two-Phase Darcy Flows in Fractured and Deformable Porous Media, Convergence Analysis and Iterative Coupling. In *Conference Proceedings, ECMOR XVII*, volume 2020, pages 1–20. European Association of Geoscientists & Engineers, 2020.

[9] F. Bonaldi, K. Brenner, J. Droniou, and R. Masson. Gradient discretization of two-phase flows coupled with mechanical deformation in fractured porous media. *Computers and Mathematics with Applications*, 98:40–68, 2021.

[10] F. Bonaldi, K. Brenner, J. Droniou, R. Masson, A. Pasteau, and L. Trenty. Gradient discretization of two-phase poro-mechanical models with discontinuous pressures at matrix fracture interfaces. *ESAIM: Mathematical Modelling and Numerical Analysis*, 55(5):1741–1777, 2021.

[11] F. Bonaldi, J. Droniou, and R. Masson. Numerical analysis of a mixed-dimensional poromechanical model with frictionless contact at matrix-fracture interfaces. Preprint arXiv:2201.09646, hal-03541096, 2022.

[12] F. Bonaldi, J. Droniou, R. Masson, and A. Pasteau. Energy-stable discretization of two-phase flows in deformable porous media with frictional contact at matrix–fracture interfaces. *Journal of Computational Physics*, 2022.

[13] W. M. Boon and J. M. Nordbotten. Mixed-dimensional poromechanical models of fractured porous media. *Acta Mechanica*, 2022.

[14] W.M. Boon, J.M. Nordbotten, and I. Yotov. Robust discretization of flow in fractured porous media. *SIAM Journal on Numerical Analysis*, 56(4):2203–2233, 2018.

[15] A. Borio, F. Hamon, N. Castelletto, J.A. White, and R.S. Settgast. Hybrid mimetic finite-difference and virtual element formulation for coupled poromechanics. *Computer Methods in Applied Mechanics and Engineering*, 383:113917, 2021.

[16] K. Brenner, M. Groza, C. Guichard, G. Lebeau, and R. Masson. Gradient discretization of hybrid-dimensional Darcy flows in fractured porous media. *Numerische Mathematik*, 134(3):569–609, 2016.

[17] K. Brenner, J. Hennicker, R. Masson, and P. Samier. Gradient Discretization of Hybrid Dimensional Darcy Flows in Fractured Porous Media with discontinuous pressure at matrix fracture interfaces. *IMA Journal of Numerical Analysis*, 37:1551–1585, 2017.

[18] D. Cerroni, L. Formaggia, and A. Scotti. A control problem approach to coulomb's friction. *Journal of Computational and Applied Mathematics*, 385:113196, 2021.

[19] F. Chave, D. A. Di Pietro, and L. Formaggia. A hybrid high-order method for Darcy flows in fractured porous media. *SIAM Journal on Scientific Computing*, 40(2):A1063–A1094, 2018.

[20] F. Chouly. An adaptation of Nitsche's method to the Tresca friction problem. *Journal of Mathematical Analysis and Applications*, 411(1):329–339, 2014.

[21] F. Chouly, M. Fabre, P. Hild, R. Mlika, J. Pousin, and Y. Renard. An overview of recent results on nitsche's method for contact problems. In Stéphane P. A. Bordas, Erik Burman, Mats G. Larson, and Maxim A. Olshanskii, editors, *Geometrically Unfitted Finite Element Methods and Applications*, pages 93–141, Cham, 2017. Springer International Publishing.

[22] F. Chouly and P. Hild. A Nitsche-based method for unilateral contact problems: numerical analysis. *SIAM Journal on Numerical Analysis*, 51(2):1295–1307, 2013.

[23] F. Chouly, P. Hild, V. Lleras, and Y. Renard. Nitsche method for contact with Coulomb friction: existence results for the static and dynamic finite element formulations. *Journal of Computational and Applied Mathematics*, 416:Paper No. 114557, 18, 2022.

[24] F. Chouly, P. Hild, and Y. Renard. Symmetric and non-symmetric variants of Nitsche's method for contact problems in elasticity: theory and numerical experiments. *Mathematics of Computation*, 84(293):1089–1112, 2015.

[25] O. Coussy. *Poromechanics*. John Wiley & Sons, 2004.

[26] E. Flauraud, F. Nataf, I. Faille, and R. Masson. Domain decomposition for an asymptotic geological fault modeling. *Comptes Rendus à l'académie des Sciences, Mécanique*, 331:849–855, 2003.

[27] B. Flemisch, I. Berre, W.M. Boon, A. Fumagalli, N. Schwenck, A. Scotti, I. Stefansson, and A. Tatomir. Benchmarks for single-phase flow in fractured porous media. *Advances in Water Resources*, 111:239–258, 2018.

[28] A. Franceschini, N. Castelletto, J.A. White, and H.A. Tchelepi. Algebraically stabilized Lagrange multiplier method for frictional contact mechanics with hydraulically active fractures. *Computer Methods in Applied Mechanics and Engineering*, 368:113161, 2020.

[29] T. T. Garipov, M. Karimi-Fard, and H. A. Tchelepi. Discrete fracture model for coupled flow and geomechanics. *Computational Geosciences*, 20(1):149–160, 2016.

[30] T.T. Garipov and M.H. Hui. Discrete fracture modeling approach for simulating coupled thermo-hydro-mechanical effects in fractured reservoirs. *International Journal of Rock Mechanics and Mining Sciences*, 122:104075, 2019.

[31] V. Girault, M.F. Wheeler, B. Ganis, and M.E. Mear. A lubrication fracture model in a poro-elastic medium. *Mathematical Models and Methods in Applied Sciences*, 25:587–645, 2015.

[32] T. Gustafsson, R. Stenberg, and J. Videman. Nitsche's method for unilateral contact problems. *Portugaliae Mathematica*, 75(3-4):189–204, 2018.

[33] T. Gustafsson, R. Stenberg, and J. Videman. Error analysis of Nitsche's mortar method. *Numerische Mathematik*, 142(4):973–994, 2019.

[34] T. Gustafsson, R. Stenberg, and J. Videman. On Nitsche's method for elastic contact problems. *SIAM Journal on Scientific Computing*, 42(2):B425–B446, 2020.

[35] T. Gustafsson and J. Videman. Stabilized finite elements for Tresca friction problem. *ESAIM. Mathematical Modelling and Numerical Analysis*, 56(4):1307–1326, 2022.

[36] A. Hansbo and P. Hansbo. A finite element method for the simulation of strong and weak discontinuities in solid mechanics. *Computer Methods in Applied Mechanics and Engineering*, 193(33-35):3523–3540, 2004.

[37] J. Haslinger, I. Hlaváček, and J. Nečas. *Numerical methods for unilateral problems in solid mechanics*, volume IV of *Handbook of Numerical Analysis (eds. P.G. Ciarlet and J.L. Lions)*. North-Holland Publishing Co., Amsterdam, 1996.

[38] J. Haslinger and T. Sassi. Mixed finite element approximation of 3D contact problems with given friction: error analysis and numerical realization. *M2AN. Mathematical Modelling and Numerical Analysis*, 38(3):563–578, 2004.

[39] P. Heintz and P. Hansbo. Stabilized Lagrange multiplier methods for bilateral elastic contact with friction. *Computer Methods in Applied Mechanics and Engineering*, 195(33-36):4323–4333, 2006.

[40] P. Hild and P. Laborde. Quadratic finite element methods for unilateral contact problems. *Applied Numerical Mathematics*, 41(3):401–421, 2002.

[41] P. Hild and Y. Renard. A stabilized lagrange multiplier method for the finite element approximation of contact problems in elastostatics. *Numerische Mathematik*, 115(1):101–129, 2010.

[42] M. Karimi-Fard, L.J. Durlofsky, and K. Aziz. An efficient discrete-fracture model applicable for general-purpose reservoir simulators. *SPE Journal*, 9(2):227–236, 2004.

[43] N. Kikuchi and J. T. Oden. *Contact problems in elasticity: a study of variational inequalities and finite element methods*, volume 8 of *SIAM Studies in Applied Mathematics*. Society for Industrial and Applied Mathematics (SIAM), Philadelphia, PA, 1988.

[44] V. Lleras. A stabilized lagrange multiplier method for the finite element approximation of frictional contact problems in elastostatics. *Mathematical Modelling of Natural Phenomena*, 4(1):163–182, 2009.

[45] V. Martin, J. Jaffré, and J. E. Roberts. Modeling fractures and barriers as interfaces for flow in porous media. *SIAM Journal on Scientific Computing*, 26:1667–1691, 2005.

[46] J. Nitsche. Über ein Variationsprinzip zur Lösung von Dirichlet-Problemen bei Verwendung von Teilräumen, die keinen Randbedingungen unterworfen sind. *Abhandlungen aus dem Mathematischen Seminar der Universität Hamburg*, 36:9–15, 1971.

[47] J.M. Nordbotten, W.M. Boon, A. Fumagalli, and E. Keilegavlen. Unified approach to discretization of flow in fractured porous media. *Computational Geosciences*, 23:225–237, 2019.

[48] A.V. Phan, J.A.L. Napier, L.J. Gray, and T. Kaplan. Symmetric-Galerkin BEM simulation of fracture with frictional contact. *International Journal for Numerical Methods in Engineering*, 57:835–851, 2003.

[49] Y. Renard. Generalized Newton's methods for the approximation and resolution of frictional contact problems in elasticity. *Computer Methods in Applied Mechanics and Engineering*, 256:38–55, 2012.

[50] T.H. Sandve, I. Berre, and J.M. Nordbotten. An efficient multi-point flux approximation method for discrete fracture-matrix simulations. *Journal of Computational Physics*, 231:3784–3800, 2012.

[51] I. Stefansson, I. Berre, and E. Keilegavlen. A fully coupled numerical model of thermo-hydro-mechanical processes and fracture contact mechanics in porous media. *Computer Methods in Applied Mechanics and Engineering*, 386:114122, 2020.

[52] R. Stenberg. On some techniques for approximating boundary conditions in the finite element method. *Journal of Computational and Applied Mathematics*, 63(1-3):139–148, 1995.

[53] X. Tunc, I. Faille, T. Gallouët, M.C. Cacas, and P. Havé. A model for conductive faults with non matching grids. *Computational Geosciences*, 16:277–296, 2012.

[54] B. I. Wohlmuth. Variationally consistent discretization schemes and numerical algorithms for contact problems. *Acta Numerica*, 20:569–734, 2011.

[55] B. I. Wohlmuth, A. Popp, M. W. Gee, and W. A. Wall. An abstract framework for a priori estimates for contact problems in 3D with quadratic finite elements. *Computational Mechanics*, 49(6):735–747, 2012.

[56] P. Wriggers. *Computational Contact Mechanics*. Springer, 2nd edition, 2006.